NTNU

Norwegian University of
Science and Technology

Higher Order Spectral method for wave scenarios with nonlinear and dispersive effects

Christopher Lawrence

Marine Technology
Submission date: June 2018
Supervisor: Marilena Greco, IMT
Co-supervisor: Jens Bloch Helmers, DNV-GL
Odin Gramstad, DNV-GL

Norwegian University of Science and Technology
Department of Marine Technology

For my mother

”He has made everything beautiful in its time.”, Ecclesiastes 3:11

NTNU Trondheim
Norwegian University of Science and Technology
Faculty of Engineering Science and Technology
Department of MarineTechnology

MASTER THESIS IN MARINE TECHNOLOGY

Spring 2018

FOR

Christopher Lawrence

Higher Order Spectral method for wave scenarios with nonlinear and dispersive effects

(Higher Order Spectral metode for bølge scenarier med ikke-lineære og dispersive effekter)

The proper prediction for ships and offshore-structure behavior at sea requires an accurate description of the incident waves and then a reliable model for the wave-body interaction problem. The features and nonlinearities of the wave systems depend on their characteristic height relative to characteristic length, on the water depth and on sea-bottom topography. There exists a variety of wave models applicable for different water depths and degree of nonlinearity. Present master thesis is the logical continuation of a project-thesis work where a higher order spectral (HOS) method was implemented within 2D framework and assessed against other numerical solutions and experiments, respectively, for a solitary wave propagating on a region with constant depth, a strong focusing wave group experiment and for propagating bi-chromatic wave experiment.

Objective

The present master thesis aims to numerically study various wave scenarios of practical relevance, and related nonlinear and dispersive features, by means of the HOS method.

The work should be carried out in steps as follows:

1. Summarize major findings/outcomes from the project thesis and complement the literature survey in order to identify state-of-the-art use of HOS and other numerical methods for phenomena involving occurrence of critical waves, e.g. freak waves, wave steepening, e.g. shoaling, and other wave scenarios governed by nonlinear and or dispersive features. For freak waves, provide the state-of-the-art of the methods/strategies to predict them, related strengths and weaknesses.
2. Extend the HOS method to handle effects of bottom topography and apply it for 2D cases to assess capability in handling wave steepening during propagation from deep to shallower water regions and compare against reference results as verification/validation of the method.
3. Calculate the water particle kinematics and make a comparison for various methods.
4. Apply the 2D HOS method to investigate the occurrence of freak waves and compare the method with others methods and against reference results as verification/validation of the method.
5. Draw the conclusions from the studies and discuss possible further steps for HOS development and possible applications.

The work may show to be more extensive than anticipated. Some topics may therefore be left out after discussion with the supervisor without any negative influence on the grading.

The candidate should in his report give a personal contribution to the solution of the problem formulated in this text. All assumptions and conclusions must be supported by mathematical models and/or references to physical effects in a logical manner.

The candidate should apply all available sources to find relevant literature and information on the actual problem.

The thesis should be organised in a rational manner to give a clear presentation of the work in terms of exposition of results, assessments, and conclusions. It is important that the text is well written and that tables and figures are used to support the verbal presentation. The thesis should be complete, but still as short as possible. In particular, the text should be brief and to the point, with a clear language. Telegraphic language should be avoided.

The thesis must contain the following elements: the text defining the scope (i.e. this text), preface (outlining project-work steps and acknowledgements), abstract (providing the summary), table of contents, main body of thesis, conclusions with recommendations for further work, list of symbols and acronyms, references and (optional) appendices. All figures, tables and equations shall be numerated.

The supervisor may require that the candidate, in an early stage of the work, present a written plan for the completion of the work. The plan should include budget for the use of computer and laboratory resources that will be charged to the department. Overruns shall be reported to the supervisor.

From the thesis it should be possible to identify the work carried out by the candidate and what has been found in the available literature. It is important to give references to the original source for theories and experimental results.

Supervisor : Marilena Greco
Co-supervisor : Jens Bloch Helmers
Co-supervisor : Odin Gramstad
Submitted : January 15th 2018
Deadline : June 11th 2018

Marilena Greco
Supervisor

Abstract

For ocean application, a High Order Spectral (HOS) method is studied. Different from most application of HOS method which use initial value problem to investigate the spectrum evolution, embedded wave generation is implemented to assess the HOS method with the wave tank experiments. The HOS method is also extended for non-uniform bathymetry to handle wave steepening during propagation from deep to shallow water. The enchancement of rogue wave occurence due to bottom topography is studied by considering irregular waves propagation over a sloping bottom. Furthermore, the increasing use of Computational Fluid Dynamics (CFD) in ship and offshore structure analysis requires an accurate water particle kinematics for the input. Therefore, the calculation of water particle kinematics is investigated.

Acknowledgement

The research presented in this thesis has been carried out over this past year in Marine technology department at NTNU, in collaboration with DNV-GL.

First, i would like to express my gratitude to my supervisor, Professor Marilena Greco for her guidance and the time for weekly meetings.

I would also like to pronounce my sincere thanks to Odin Gramstad and Jens Bloch Helmers for giving me an opportunity to visit DNV-GL headquarters and for all valuable discussions.

I acknowledge Labmath-Indonesia (LMI) for the academic license of HAWASSI-VBM. I thank Carl Trygve Stansberg from MARINTEK (now SINTEF Ocean) for providing me experiment data. I also thank MARIN, Netherlands for the use of the data and other scientists who published their experimental results used in this thesis.

I am indebted to Professor E. van Groesen (Brenny) for trusting me to publish paper in international journal as first author. I thank him for introducing me the beautiful of mathematics and physics in water waves.

I wish to express my thanks to Dr. Andonowati for providing me a nice place for research at LMI. In LMI, I made a lot of friends with whom i can share everything. I thank Didit, Ruddy, Andreas, Mourice, Peri, Nugrahinggil, Abrari, Januar, Alif and others.

I thank Professor Sri Redjeki Pudjaprasetya and her group for all fruitful discussion that we had during my bachelor degree. I took my first course with her in partial differential equations. From there, i was fascinated with her works in mathematics. She gave me a lot of motivation to continue my research in applied mathematics. I thank for her caring, i am really glad to meet her.

I am really grateful for being surrounded by many warm-hearted people during my stay in Trondheim, Norway. I wish to express my thanks to all member of Indonesian Student Association in Trondheim (PPIT) and also all Indonesian family in Trondheim whom i cannot name one by one. I am also very thankful to my flatmate, Devina Anisa, which made my stay in Trondheim enjoyable.

I am grateful to my family especially my two big brothers : Albert Wijaya and Teguh Lesmana. I am truly grateful to my parents, Suyanto Tan and Susanti Wijaya for their support. Last but not least, i would like to thank Yemima Tanudjaja for always loving me and being patient with me. Thanks for everything.

Table of Contents

Abstract i

Acknowledgement iii

Table of Contents v

List of Tables vii

List of Figures ix

Nomenclature xiii

1 Introduction 1
- 1.1 Background and motivation . . . 1
- 1.2 Mechanism of rogue waves . . . 2
- 1.3 Outline . . . 3

2 Hamiltonian Wave Modelling 5
- 2.1 Consistent Hamiltonian modeling . . . 6
  - 2.1.1 Shallow Water Equations . . . 6
  - 2.1.2 High Order Spectral method . . . 7
  - 2.1.3 Variational Boussinesq model . . . 10
- 2.2 Embedded wave generation . . . 12
- 2.3 Numerical implementation . . . 14
  - 2.3.1 Spatial discretization . . . 14
  - 2.3.2 Initialization and time stepping . . . 16
  - 2.3.3 Nonlinear adjustment and damping zones . . . 17

3 Higher Order Spectral Method on Variable Depth 19
- 3.1 Original method . . . 19
- 3.2 Hybrid spatial spectral method . . . 21
  - 3.2.1 Limiting cases . . . 22

3.2.2 HOS method with hybrid spatial spectral method 23

4 Numerical Investigation **25**
4.1 Solitary wave propagation over flat bottom 25
4.2 Bichromatic wave train experiment 26
4.3 Focusing wave group experiment 32
4.4 Regular and irregular waves over a submerged bar 34
4.5 Irregular waves over a sloping bottom 37
4.5.1 Comparison with laboratory experiments 38
4.5.2 Effects of the bottom slope and water depth 38

5 Calculation of Water Particle Kinematics **45**
5.1 H and H_2 operator 45
5.2 Variational Boussinesq Model 46
5.3 Nonlinear Extension of Airy Theory 46
5.4 Validation 47

6 Conclusion and recommendations **53**
6.1 Conclusion 53
6.2 Recommendations 54

Bibliography **55**

Appendix **59**
A Supplementary of simulation results 59

List of Tables

4.1 Comparison of correlation and variance-quotient for HOS method up to 7th order in solitary wave propagation case. 26
4.2 Wave properties for bichromatic wave train experiment 27
4.3 Correlation and Variance-quotient for HOS third order simulation in bichromatic wave experiment. 32
4.4 Statistical properties and computational relative time for irregular waves over submerged bar simulation using Original method with $M_b = 3$ and $M_b = 5$. 36
4.5 Statistical properties and computational relative time for irregular waves over submerged bar simulation using Hybrid spatial spectral method. . . . 36
4.6 Parameters of the wave-fields in MARIN experiment 38
4.7 Parameters for irregular wave propagation over a sloping bottom simulation. Subscript 1 indicate deeper region, and subscript 2 indicate shallower region. 39

List of Figures

1.1 The time series of the New Year Wave, recorded at the Draupner platform in the North sea on January 1st, 1995. Haver (2000) 2

2.1 Characteristic smooth functions for damping zones (blue, solid) and non-linear adjustment (red, solid) with influx position at $x = 10$ m. 18

4.1 The initial wave elevation (upper plot) and velocity potential (lower plot) of the solitary wave with height of 0.7 m. 26
4.2 Comparison for solitary wave simulation between FN-VBM (blue, dash) and HOS up to 7th order (red, solid) at t = 20 s. 27
4.3 Simulation results of the HOS third order (red, solid) and the Maximum Temporal Crest (black, solid) at t = 10, 25, 40 s. 28
4.4 Sketch of the wave tank with the location of wave gauges. 28
4.5 Comparison of wave elevation (upper plot) and amplitude spectrum (lower plot) for bichromatic wave train experiment between HOS third order (red, dash) and measurement (blue,solid) at position W2 ($x = 40$ m). 29
4.6 Same as Figure 4.5. Now at position W3 ($x = 80$ m). 30
4.7 Same as Figure 4.5. Now at position W4 ($x = 120$ m). 30
4.8 Same as Figure 4.5. Now at position W5 ($x = 160$ m). 31
4.9 Same as Figure 4.5. Now at position W6 ($x = 200$ m). 31
4.10 The influx signal (upper plot) and the amplitude spectrum (lower plot) of the focusing wave group experiment 32
4.11 Comparison of wave elevation (upper plot) and amplitude spectrum (lower plot) for focusing wave group experiment between HOS first order (red, dash) and measurement (blue, solid) at $x = 50$ m. 33
4.12 Comparison of wave elevation (upper plot) and amplitude spectrum (lower plot) for focusing wave group experiment between HOS third order (red, dash) and measurement (blue, solid) at $x = 50$ m. 34

4.13 Spatial wave profiles for HOS first order (blue, solid), and for HOS third order (red, solid) at time t = 94.2 s and the Maximum Temporal Amplitudes for HOS first order (blue, dash) and HOS third order (red, dash). 34
4.14 Bottom profile of the experiment of Beji and Battjes (1993). 35
4.15 Comparison for harmonic wave over a submerged bar experiment between second order HOS method with hybrid spatial spectral method (red, dashed) and measurement (blue, solid). 37
4.16 Convergence of the ensemble-averaged kurtosis and skewness with respecto to number of runs in the ensemble for case 2. 39
4.17 Kurtosis and skewness for the experimental case 1. Black circles: experimental results reported by Trulsen et al. (2012), solid line: numerical simulations. 40
4.18 Same as Figure 4.17 for experimental case 2. 40
4.19 Same as Figure 4.17 for experimental case 3. 41
4.20 Kurtosis and skewness for different slope length cases, i.e. Case I-IV. . . . 42
4.21 Kurtosis and skewness for different water depth cases, i.e. Case V-VIII. . 42
4.22 Probability of rogue waves for case I-IV. 43
4.23 Probability of rogue waves for case V-VIII. 43

5.1 Comparison of horizontal velocity at $z = 0$ betwen H and H_2 operator with exact solution. The H_2 operator is performed by two steps. 48
5.2 Same as Figure 5.1, now for vertical velocity 48
5.3 Convergence of horizontal velocity with respect to number of steps in H_2 operator for different degrees of nonlinearity. 49
5.4 Same as Figure 5.3, now for vertical velocity. 49
5.5 Horizontal velocity profile of a solitary wave by using H_2 operator. 50
5.6 Vertical velocity profile of a solitary wave by using H_2 operator. 50
5.7 Comparison of horizontal and velocity at $z = 0$ between VBM method and exact solution. 51
5.8 Comparison of vertical velocity at surface between nonlinear extension of airy theory and exact solution. 51

A.1 Comparison of wave elevation (upper plot) and amplitude spectrum (lower plot) for bichromatic wave train experiment between HOS first order (red, dash) and measurement (blue,solid) at position W2 ($x = 40$ m). 59
A.2 Same as Figure A.1. Now at position W3 ($x = 80$ m). 60
A.3 Same as Figure A.1. Now at position W4 ($x = 120$ m). 60
A.4 Same as Figure A.1. Now at position W5 ($x = 160$ m). 61
A.5 Same as Figure A.1. Now at position W6 ($x = 200$ m). 61
A.6 Comparison of wave elevation (upper plot) and amplitude spectrum (lower plot) for bichromatic wave train experiment between HOS second order (red, dash) and measurement (blue,solid) at position W2 ($x = 40$ m). . . . 62
A.7 Same as Figure A.6. Now at position W3 ($x = 80$ m). 62
A.8 Same as Figure A.6. Now at position W4 ($x = 120$ m). 63
A.9 Same as Figure A.6. Now at position W5 ($x = 160$ m). 63

A.10 Same as Figure A.6. Now at position W6 ($x = 200$ m). 64
A.11 Comparison of wave elevation for focusing wave group experiment between HOS 3rd order (red, dash) at $x = 50.2$ m and measurement (blue, solid) at $x = 50$ m. 65
A.12 Comparison of wave elevation for irregular waves over a submerged bar experiment between HOS second order (red, dash) and measurement (blue, solid) at position W2. 66
A.13 Same as Figure A.12, now at position W3. 66
A.14 Same as Figure A.12, now at position W4. 67
A.15 Same as Figure A.12, now at position W5. 67
A.16 Same as Figure A.12, now at position W6. 68
A.17 Same as Figure A.12, now at position W7. 68

Nomenclature

H_{max}	Maximum of zero-crossing wave height
C_{max}	Maximum crest height
H_s	Significant wave height
ρ	Mass density of fluid
Φ	Velocity potential
ϕ	Velocity potential at surface
h	Mean water depth
ξ	Bottom variation
η	Surface elevation
n_B	Normal vector at the bottom
W	Fluid particle velocity in vertical direction at surface
U	Fluid particle velocity in horizontal direction at surface
N_s	Normal vector at water surface
p	Bernoulli pressure
a	Wave amplitude
g	Gravitational acceleration
k	Wave number
ω	Angular frequency
C	Phase velocity
V	Group velocity
$\mathcal{P}$	Potential energy
$\mathcal{K}$	Kinetic energy
$\mathcal{H}$	Hamiltonian / total energy
$\mathcal{L}$	Lagrangian density
F	Vertical shape functions in VBM
Ψ	Spatially dependent functions in VBM
α	Matrix in VBM equation
γ	Matrix in VBM equation
β	Vector in VBM equation
κ	Parameter in normalized hyperbolic-cosine vertical profile
T	Piecewise linear spline basis function
χ	Characteristic function for nonlinear adjustment or damping zones
M	Nonlinear order of HOS method for free surface boundary condition
M_b	Nonlinear order of HOS method in original method for bottom boundary condition

Chapter 1

Introduction

1.1 Background and motivation

For centuries, the occurence of extreme waves in ocean have been reported by sailors and scientists thought that was a myth. In the report of ESA News 21 July 2004, this extreme waves are believed to be the main cause of the sinking more than 200 supertankers and container ships in the last two decades. This extreme waves are also known as rogue, freak, monster, giant, or abnormal waves. This type of accidents are often reported in media and this extreme events have caught attention both in industry and scientific community.

There is no unique definition of rogue wave. A common definition is to apply the criteria by Haver (2000):

$$\frac{H_{max}}{H_s} > 2 \quad \text{and/or} \quad \frac{C_{max}}{H_s} > 1.25$$

where H_{max} denotes the maximum of zero-crossing wave height, C_{max} is the maximum crest height, and H_s is the significant wave height.

The first scientific evidence of rogue waves is the New Year wave or also known as Draupner Wave. On 1st January 1995, hurricane winds were blowing and extreme waves were hitting the rig. It was recorded by a laser-based rangefinder and measured 26 m from trough to peak (see Figure 1.1). The significant wave height was 10.8 m and according to statistics, such an event was possible only once every 10,000 years. This was the turning point of the study on rogue waves. Many scientists around the world started to investigate and analyze this rogue waves by using numerical models.

Nowadays, the measurements from oil rigs, satellites, or marine radar have confirmed the existence of rogue waves. Nevertheless, a lot of open questions still remain: how often a rogue wave happens, should these waves be accounted for in design, what is the best way to take rogue waves into account for design.

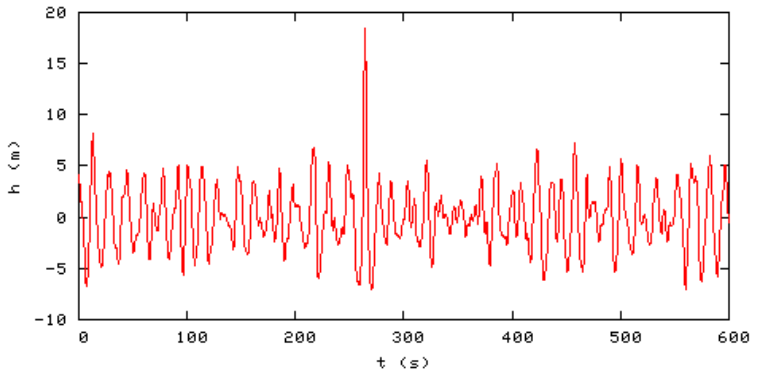

Figure 1.1: The time series of the New Year Wave, recorded at the Draupner platform in the North sea on January 1st, 1995. Haver (2000)

1.2 Mechanism of rogue waves

In the annual review of rogue waves by Dysthe et al. (2008), several physical mechanism of rogue waves are discussed: spatial focusing, dispersive focusing, and nonlinear focusing.

Spatial focusing is occured by shoaling and refraction of waves due to varying bottom. As water waves are transmitted from deep water into shallow water, the wavelength will be reduced and the wave height become higher. Another consequence is the direction of the waves can be changed depends on the bottom topography, this phenomena is called refraction. Several wave tank experiments have been conducted to see this physical mechanism of spatial focusing wave, for example wave propagation over a shoal by Berkhoff et al. (1982). Another possibility is from the wave-current interaction. A wave propagating against the current going in the opposite direction gathers energy and amplify the wave height.

Dispersive focusing is achieved by linear effect and occured when the phase from different wave frequency is the same. The dispersion means the long waves travel faster than shorter waves. Dispersive focusing can be explained from wave tank experiment by creating a long wave group with linearly decreasing frequency, then the wave group can be designed to be focused at a certain position. Another way to observe this phenomena is by running long time linear simulation of wave model for a broad band spectrum, e.g. JONSWAP spectrum. This type of focusing has been suggested in Kharif and Pelinovsky (2003) as a possible mechanism for exceptional rogue waves.

Nonlinear focusing has been researched actively for past few decades. Starting from Benjamin and Feir (1967) observation in laboratory tank, a modulational instability of nonlinear waves can lead to a extremely high wave. This is known as Benjamin-Feir instability (BF instability). Alber (1978) showed that the BF instability is only for narrow band random wave field and it can be neglected for a broad band spectrum. However, Gramstad (2017) discussed about the modulational instability for the JONSWAP spectrum and this show that this phenomenon is still an open discussion. While the instability develops, the occurence of rogue waves increase, but Gramstad and Trulsen (2007) stated that this only

occurs for long-crested waves. The nonlinear focusing can also be observed in wave tank experiment, the initial spectrum will be deformed and the growth of the nonlinear bound waves in the spectrum tail will contribute to a freak wave formation.

1.3 Outline

This report consists of an introduction, four main chapters, conclusion and recommendations, and an appendix.

In Chapter 2, Hamiltonian structure for water waves is discussed. Subsequently, the High Order Spectral (HOS) method approximate the kinetic energy with consistent order and possess the Hamiltonian structure. To study the nonlinearity of HOS method, a wave model from HAWASSI (Hamiltonian Wave-Ship-Structure Interaction) software which is Variation Boussinesq model (VBM) is used for comparison. Embedded wave generation is described briefly. The pseudo spectral implementation for HOS method and finite element implementation for VBM are given in this chapter.

In Chapter 3, HOS method is extended to deal with varying bathymetry with two different methods.

In Chapter 4, several numerical and experimental cases are selected to assess the dispersion and nonlinearity of HOS method. Effect of non-uniform bathymetry into the rogue wave occurence is studied in this chapter.

In Chapter 5, three different methods to calculate water particle kinematics are described. Furthermore, each method is tested against a reference results.

Conclusions and recommendations for future work are covered in the final chapter. Some additional simulation results are presented in appendix.

Chapter 2

Hamiltonian Wave Modelling

The mathematical-physical description of surface water waves for an incompressible and irrotational flow has a Hamiltonian structure, as discovered by Zakharov (1968) for waves on infinite depth, rediscovered by Broer (1974) for waves above a flat bottom, and verified by Miles (1977) through Luke variational principle.

The Hamiltonian is the total energy which is the sum of the potential energy and kinetic energy. The potential energy which is only depends on η is given by

$$\mathcal{P}(\eta) = \int_{\mathbf{x}} \frac{1}{2} g\eta^2 d\mathbf{x}.$$

The kinetic energy is given by

$$\mathcal{K}(\Phi) = \int_{\mathbf{x}} \int_{-h}^{\eta} \frac{1}{2} \left[(\nabla\Phi) \cdot (\nabla\Phi) + (\partial_z \Phi)^2 \right] dz d\mathbf{x} \tag{2.1}$$

with constraints as follow :

- The velocity potential Φ satisfies the Laplace equation in the fluid interior because of the incompressible and irrotational flow.
- The impermeability of the bottom leads to the condition for velocity component normal to the bottom, i.e. $\partial_n \Phi = 0$ at $z = -h(x)$.
- The velocity potential at the surface is $\Phi(\mathbf{x}, z = \eta, t) = \phi(\mathbf{x}, t)$.

Note that ∇ is the horizontal gradient (∂_x, ∂_y). These constraints are direct consequences from the requirement of variational derivative of Hamiltonian $\mathcal{H}$ with respect to Φ is zero. In other words, these conditions can be achieved by minimizing the kinetic energy as stated by Dirichlet's principle.

$$\frac{\delta \mathcal{H}}{\delta \Phi} = 0$$

Therefore, the Hamiltonian can be written as functional of the two canonical variables η and ϕ as

$$\mathcal{H}(\eta, \phi) = \mathcal{K}(\eta, \phi) + \mathcal{P}(\eta).$$

The dynamics of the canonical variables $\eta(\mathbf{x}, t)$ and $\phi(\mathbf{x}, t)$ or well known as Hamiltonian equations is given by (Zakharov (1968), Broer (1974), Miles (1977))

$$\begin{aligned} \partial_t \eta &= \delta_\phi \mathcal{H}(\eta, \phi) \\ \partial_t \phi &= -\delta_\eta \mathcal{H}(\eta, \phi). \end{aligned} \tag{2.2}$$

It turned out that there is a connection between the Hamiltonian formulation and the variational formulation in Lagrangian density $\mathcal{L}(\eta, \Phi)$ by Luke (1967):

$$\mathcal{L} = -\int \left[\int_{\mathbf{x}} \int_{-h}^{\eta} \left\{ \partial_t \Phi + \frac{1}{2} (\nabla \Phi)^2 + \frac{1}{2} (\partial_z \Phi)^2 + gz \right\} dz d\mathbf{x} \right] dt.$$

By integrating out the $\partial_t \Phi$ to the boundary of the time domain using Leibniz integral rule and dropping dynamically uninteresting terms, Miles (1977) showed the Lagrangian can be expressed as

$$\mathcal{L} = \int \left[\int \phi \partial_t \eta d\mathbf{x} - \mathcal{H}(\eta, \phi) \right] dt \tag{2.3}$$

The variation of $\mathcal{L}$ with respect to η and ϕ leads to Hamiltonian equations which satisfy incompressible Euler equations.

2.1 Consistent Hamiltonian modeling

In this section, it will be shown that several wave model can be derived consistently through the hamiltonian. It is important to aware that even shallow water equations possess the hamiltonian structure.

2.1.1 Shallow Water Equations

The shallow water equations (SWE) can be derived through Hamiltonian formulation. Here, shallow water means the wavelength is much larger than the water depth. Since the flow is mainly uniform in horizontal direction and the variations in the vertical direction may be neglected therefore it is logical to assume that $\Phi = \phi$. Inserting this assumption into Equation (2.1), the Hamiltonian equations become

$$\begin{aligned} \partial_t \eta &= -\nabla \cdot [(h + \eta) \nabla \phi] \\ \partial_t \phi &= -g\eta - \frac{1}{2} |\nabla \phi|^2. \end{aligned} \tag{2.4}$$

These are the shallow water equations (SWE). Note that the equations are fully nonlinear but do not possess the property of dispersion, i.e. all linear waves propagate with the same velocity.

Linear Shallow Water Equations

By neglecting all the nonlinear terms in Equation (2.4), we get the linear shallow water equations (LSWE) as

$$\begin{aligned} \partial_t \eta &= -h\nabla^2 \phi \\ \partial_t \phi &= -g\eta. \end{aligned} \tag{2.5}$$

This set of two first order equations in time is coupled. Decouple these equations lead to second order equation in surface elevation η only. Notice, this is the well-known wave translation equation:

$$\partial_t^2 \eta = C^2 \nabla \cdot \nabla \eta \tag{2.6}$$

where C is the phase velocity of shallow water equation. For flat bottom $h = h_0$, the phase velocity is $C_0 = \sqrt{gh_0}$ which show the long wave character of the equations.

2.1.2 High Order Spectral method

By utilizing Green's theorem, the kinetic energy in Equation (2.1) can be expressed as

$$\mathcal{K}(\eta, \phi) = \frac{1}{2} \int \phi \partial_n \Phi d\mathbf{x}$$

where $\partial_n \Phi = \partial_z \Phi(\mathbf{x}, \eta) - \nabla\eta \cdot \nabla\Phi(x, \eta)$ is the normal velocity at the surface, so-called Dirichlet to Neumann (DtN) operator. For convenience, denote W is the vertical velocity at the surface, $W = \partial_z \Phi(\mathbf{x}, \eta)$. Since $\nabla\Phi(x, \eta) = \nabla\phi - W\nabla\eta$, then the kinetic energy can be rewritten as

$$\mathcal{K}(\eta, \phi) = \frac{1}{2} \int \phi \left(W(1 + |\nabla\eta|^2) - \nabla\eta \cdot \nabla\phi \right) d\mathbf{x}.$$

Taking the first variations of the Hamiltonian $\mathcal{H}$ with respect to surface potential ϕ leads to the continuity equation. As shown by Zakharov (1968), the continuity equation is expressed by DtN operator as

$$\partial_t \eta = \delta_\phi \mathcal{H} = \partial_n \Phi.$$

Moreover, taking variations of the Hamiltonian $\mathcal{H}$ with respect to surface elevation η leads to the momentum equation or the Bernoulli equation.

$$\partial_t \phi = -\delta_\eta \mathcal{H} = -g\eta - \frac{1}{2} \left(|\nabla\Phi(x, \eta)|^2 + W^2 \right) + W\partial_n \Phi$$

Rewrite these two equations in term of surface variable only, the dynamic of Hamiltonian equations is given as follow

$$\begin{aligned} \partial_t \eta &= W(1 + |\nabla\eta|^2) - \nabla\eta \cdot \nabla\phi \\ \partial_t \phi &= -g\eta - \frac{1}{2} |\nabla\phi|^2 + \frac{1}{2} W^2 (1 + |\nabla\eta|^2). \end{aligned} \tag{2.7}$$

The solution of Equation (2.7) depends on obtaining the vertical surface velocity W in terms of η and ϕ. An efficient recursive spectral method for evaluating W was proposed

by Dommermuth and Yue (1987) and West et al. (1987) simultaneously, and has been known as the Higher Order Spectral (HOS) method. In the following, the solution procedure of HOS method is described.

Expansion of the velocity potential $\Phi(\mathbf{x}, z, t)$ and the vertical surface velocity W in power series of η give

$$\Phi(\mathbf{x}, z, t) = \sum_{m=1}^{\infty} \Phi^{(m)}(\mathbf{x}, z, t) \tag{2.8}$$

$$W(\mathbf{x}, t) = \sum_{m=1}^{\infty} W^{(m)}(\mathbf{x}, t)$$

where m shows the order of η. Further, using taylor expansion on each terms $\Phi^{(m)}$ and $W^{(m)}$ around the still water elevation $z = 0$:

$$\Phi^{(m)}(\mathbf{x}, z = \eta, t) = \sum_{n=0}^{\infty} \frac{\eta^n}{n!} \frac{\partial^n \Phi^{(m)}}{\partial z^n}(\mathbf{x}, 0, t) \tag{2.9}$$

$$\begin{aligned} W^{(m)}(\mathbf{x}, t) &= \left. \frac{\partial \Phi^{(m)}}{\partial z} \right|_{z=\eta} \\ &= \sum_{n=0}^{\infty} \frac{\eta^n}{n!} \frac{\partial^{n+1} \Phi^{(m)}}{\partial z^{n+1}}(\mathbf{x}, 0, t). \end{aligned}$$

From Equation (2.8) and (2.9), the surface potential ϕ can be expressed as

$$\phi(\mathbf{x}, t) = \Phi(\mathbf{x}, \eta, t) = \sum_{m=1}^{\infty} \sum_{n=0}^{\infty} \frac{\eta^n}{n!} \frac{\partial^n \Phi^{(m)}}{\partial z^n}(\mathbf{x}, 0, t) \tag{2.10}$$

Classifying the left hand side and right hand side of Equation (2.10) based on the same order results in a triangular system for $\Phi^{(m)}$

$$\begin{aligned} \phi &= \Phi^{(1)} \\ 0 &= \eta \frac{\partial \Phi^{(1)}}{\partial z} + \Phi^{(2)} \\ 0 &= \frac{\eta^2}{2} \frac{\partial^2 \Phi^{(1)}}{\partial z^2} + \eta \frac{\partial \Phi^{(2)}}{\partial z} + \Phi^{(3)} \\ 0 &= \frac{\eta^3}{6} \frac{\partial^3 \Phi^{(1)}}{\partial z^3} + \frac{\eta^2}{2} \frac{\partial^2 \Phi^{(2)}}{\partial z^2} + \eta \frac{\partial \Phi^{(3)}}{\partial z} + \Phi^{(4)} \\ 0 &= \sum_{n=1}^{m} \frac{\eta^{n-1}}{(n-1)!} \frac{\partial^{n-1} \Phi^{(m-n+1)}}{\partial z^{n-1}}. \end{aligned} \tag{2.11}$$

Rearrange Equation (2.11) gives the following velocity potential solution at $z = 0$ for each order explicitly :

$$\begin{aligned}
\Phi^{(1)} &= \phi \\
\Phi^{(2)} &= -\eta \frac{\partial \Phi^{(1)}}{\partial z} \\
\Phi^{(3)} &= -\frac{\eta^2}{2}\frac{\partial^2 \Phi^{(1)}}{\partial z^2} - \eta \frac{\partial \Phi^{(2)}}{\partial z} \\
\Phi^{(4)} &= -\frac{\eta^3}{6}\frac{\partial^3 \Phi^{(1)}}{\partial z^3} - \frac{\eta^2}{2}\frac{\partial^2 \Phi^{(2)}}{\partial z^2} - \eta \frac{\partial \Phi^{(3)}}{\partial z} \\
\Phi^{(m)} &= -\sum_{n=1}^{m-1} \frac{\eta^n}{n!} \frac{\partial^n \Phi^{(m-n)}}{\partial z^n}.
\end{aligned} \tag{2.12}$$

In the same way, we obtain the vertical surface velocity W for each order in the form :

$$\begin{aligned}
W^{(1)} &= \frac{\partial \Phi^{(1)}}{\partial z} \\
W^{(2)} &= \eta \frac{\partial^2 \Phi^{(1)}}{\partial z^2} + \frac{\partial \Phi^{(2)}}{\partial z} \\
W^{(3)} &= \frac{\eta^2}{2}\frac{\partial^3 \Phi^{(1)}}{\partial z^3} + \eta \frac{\partial^2 \Phi^{(2)}}{\partial z^2} + \frac{\partial \Phi^{(3)}}{\partial z} \\
W^{(4)} &= \frac{\eta^3}{6}\frac{\partial^4 \Phi^{(1)}}{\partial z^4} + \frac{\eta^2}{2}\frac{\partial^3 \Phi^{(2)}}{\partial z^3} + \eta \frac{\partial^2 \Phi^{(3)}}{\partial z^2} + \frac{\partial \Phi^{(4)}}{\partial z} \\
W^{(m)} &= \sum_{n=0}^{m-1} \frac{\eta^n}{n!} \frac{\partial^{n+1} \Phi^{(m-n)}}{\partial z^{n+1}}.
\end{aligned} \tag{2.13}$$

Dommermuth and Yue (1987) approximate the terms related with vertical surface velocity in Equation (2.7) with

$$\begin{aligned}
W\left(1 + |\nabla\eta|^2\right) &\approx \sum_{m=1}^{M} \left[W^{(m)} \left(1 + |\nabla\eta|^2\right) \right] \\
\frac{1}{2} W^2 \left(1 + |\nabla\eta|^2\right) &\approx \sum_{m=1}^{M} \left[\frac{1}{2} \left(W^{(m)} \right)^2 \left(1 + |\nabla\eta|^2\right) \right]
\end{aligned}$$

On the other hand, according to West et al. (1987) these terms need to be truncated at consistent nonlinear order to possess Hamiltonian structure,

$$\begin{aligned}
W\left(1 + |\nabla\eta|^2\right) &\approx W^{(1)} + W^{(2)} + \sum_{m=3}^{M} \left[\left(W^{(m)} + W^{(m-2)} |\nabla\eta|^2 \right) \right] \\
W^2 \left(1 + |\nabla\eta|^2\right) &\approx \sum_{m=2}^{M} \left(W^2 \right)^{(m)} + \sum_{m=4}^{M} \left(W^2 \right)^{(m-2)} |\nabla\eta|^2
\end{aligned}$$

with

$$(W^2)^{(m)} = \sum_{n=1}^{m} W_n W_{m-n}.$$

For clarity, the dynamic equations of HOS method up to fourth order based on West et al. (1987) are given as

$$\begin{aligned}\partial_t \eta \;=\; & W^{(1)} + \left(W^{(2)} - \nabla\phi\cdot\nabla\eta\right) \\ & + \left(W^{(3)} + W^{(1)}\left|\nabla\eta\right|^2\right) + \left(W^{(4)} + W^{(2)}\left|\nabla\eta\right|^2\right)\end{aligned}$$

$$\begin{aligned}\partial_t \phi \;=& -g\eta + \left(-\frac{\left|\nabla\phi\right|^2}{2} + \frac{W^{(1)}W^{(1)}}{2}\right) \\ & + \left(W^{(1)}W^{(2)}\right) + \left(\frac{W^{(2)}W^{(2)} + 2W^{(1)}W^{(3)}}{2} + \frac{W^{(2)}W^{(2)}}{2}\left|\nabla\eta\right|^2\right)\end{aligned}$$

Terms of the same order have been grouped together in the bracket.

2.1.3 Variational Boussinesq model

The Variational Bussinesq model (VBM) is under HAWASSI (Hamiltonian Wave-Ship-Structure Interaction) software license. The HAWASSI-VBM is for simulations of long (1HD) and short crested waves (2HD) with excellent dispersion properties in coastal areas with harbours and strongly varying bathymetry, and for simulation of oceanic waves.

Starting from Klopman et al. (2010), the velocity potential $\Phi(\mathbf{x}, z, t)$ is extended by adding z-dependence functions.

$$\Phi\left(\mathbf{x}, z, t\right) = \phi\left(\mathbf{x}, t\right) + \Sigma_m F_m\left(z, \eta, h\right)\psi_m\left(\mathbf{x}, t\right) = \phi + F\cdot\Psi \tag{2.14}$$

where F_m are vertical shape functions that will be chosen in advance and ψ_m are spatially dependent functions that need to be determined by minimizing the kinetic energy with respect to ψ_m.

Substituting Equation (2.14) into kinetic energy functional results in

$$\begin{aligned}K_{VBM} &= \frac{1}{2}\int_{\mathbf{x}}\int_{-h}^{\eta}\left|\nabla\phi + \nabla\left(F\cdot\Psi\right)\right|^2 + \left(\partial_z F\cdot\Psi\right)^2\, dzd\mathbf{x} \\ &= \frac{1}{2}\int_{\mathbf{x}}\int_{-h}^{\eta}\left|\nabla\phi + F\cdot\nabla\Psi + \nabla F\cdot\Psi\right|^2 + \left(\partial_z F\cdot\Psi\right)^2\, dzd\mathbf{x}\end{aligned} \tag{2.15}$$

Neglecting the effects of variations of F with x, i.e. $\nabla F = 0$, leads to weakly nonlinear VBM (see Klopman et al. (2010), Lakhturov et al. (2012), Adytia and van Groesen (2012)). Taking all terms in Equation (2.15) into account will produce fully nonlinear VBM, without approximation for the nonlinearity. The derivation of fully nonlinear VBM

is described in Lawrence et al. (2018). In this project report, we only derive for linear VBM to show the linear dispersion of the model.

For convenience, matrices α and γ, and a vector β are introduced as

$$\alpha_{ij} = \int_{-h}^{0} F_i F_j dz, \quad \gamma_{ij} = \int_{-h}^{0} F_i' F_j' dz, \quad \beta_i = \int_{-h}^{0} F_i dz \tag{2.16}$$

Using this notation, the kinetic energy of linear VBM is rewritten as

$$K_{VBM} = \frac{1}{2} \int_{\mathbf{x}} \left[h \left| \nabla \phi \right|^2 + \alpha \nabla \Psi \cdot \nabla \Psi + \gamma \Psi \cdot \Psi + 2 \nabla \phi \beta \cdot \nabla \Psi \right] d\mathbf{x} \tag{2.17}$$

The dynamic equations of VBM is found by taking variations of Hamiltonian of VBM with respect to η and ϕ . Meanwhile, the functions Ψ are calculated by minimizing kinetic energy of VBM with respect to Ψ, leading to a system of linear elliptic equations. Hence, the linear VBM equations are as follows

$$\begin{aligned} \partial_t \eta &= -h \nabla^2 \phi - \beta \nabla \cdot \nabla \Psi \\ \partial_t \phi &= -g \eta \\ \alpha \nabla \cdot \nabla \Psi + \gamma \Psi &= \beta \nabla \cdot \nabla \phi \end{aligned} \tag{2.18}$$

VBM linear dispersion relation

The VBM with multiple profiles has dispersion relation that depends on the choice of vertical shape functions. The linear VBM dispersion is given as

$$\Omega_{VBM}(k) = c_0 k \sqrt{1 - \frac{k^2}{h} \beta \cdot (\alpha k^2 + \gamma)^{-1} \beta}.$$

Vertical profile optimization

Several type of vertical shape functions were discussed in Klopman (2010). By choosing a parabolic profile as in Equation (2.19), it gives the same quality of dispersion as the Boussinesq model of Madsen et al. (1991) which is good only for long waves or up to $kh \approx 3$.

$$F_1(z, \eta, h) = \frac{1}{2}(z - \eta) \frac{2h + z + \eta}{h + \eta} \tag{2.19}$$

For multiple profile, Adytia (2012) used the normalized hyperbolic-cosine vertical profile and adjusted to satisfy $F_m(z = \eta) = 0$

$$F_m\left(z, \eta, h\right) = \frac{\cosh\left(\kappa_m \left(z + h\right)\right)}{\cosh\left(\kappa_m \left(\eta + h\right)\right)} - 1 \tag{2.20}$$

Here the parameters κ_m are constants that can be optimized to improve the dispersion quality. For waves with a narrow band spectrum, e.g. monochromatic waves, it is enough to choose one profile with parameter κ is wave number that corresponds with frequency

of the monochromatic waves. Another example, for bichromatic waves that travel with frequency ω_1 and ω_2, two profiles should be used with parameters κ_1 and κ_2 are wave number that correspond with frequency ω_1 and ω_2, respectively. For broad band spectrum, it is recommended to use multiple profiles. Lakhturov et al. (2012) use kinetic energy minimization based on power spectrum of the influx signal. Later, Lawrence et al. (2018) found that the initial spectrum will deform during the evolution when strong nonlinear effects are present and the optimization should be based on deformed spectrum.

2.2 Embedded wave generation

There are two ways to study the evolution of water waves by utilizing the wave model.

First, the initial value problem, i.e. the description of the surface elevation η and surface potential ϕ at initial time instant are chosen. Ideally, these initial conditions should be chosen consistently through their nonlinear relationship which represent the bound wave components correctly. However, these nonlinear relationship is complicated therefore most applications use linear relationship between η and ϕ. Notice that the typical model spectrum such as JONSWAP spectrum is calibrated from measurement in the North Sea which is already contain the bound waves. Therefore, using linear relationship for a JONSWAP spectrum means the free wave components is overpredicted and may lead to excess energy in the spectrum tail. Lack of consistent initialization by linear relationship, may lead to instabilities with high frequency spurious modes in the simulations. To remedy this problem, Dommermuth (2000) proposed an adjustment scheme in time where the nonlinear terms in the equations are turned on gradually.

The second one is influxing problem. The condition is different with the initial value problem when the waves have to be excited from the boundary or inside the domain. For instance, evolution of the waves that is generated by the wavemaker in a hydrodynamic laboratory or waves propagation from offshore to nearshore. Engquist and Majda (1977) describe the wave generation from the boundary with phase speed. However, it is important to ensure the reflected waves should be able to pass through the influx boundary which is way too complicated because the natural boundary of the wave model. On the contrary, in Wei et al. (1999) the waves is generated from the vertical line under an angle theta with respect to x-axis. They used a spatially distributed source function method (Gauss shape function) to generate waves inside the domain for nonlinear shallow water equations, the classical Boussinesq model of Peregrine (1967), extended Boussinesq model of Nwogu (1993), and in the fully nonlinear form Wei and Kirby (1995). Kim et al. (2007) showed that it is possible to generate oblique waves by using a delta source function and argued that the group velocity of the wave model plays an important role. Liam et al. (2014) derived the embedded wave generation in a general way for any linear dispersive wave models.

For the influx problems in this project report, we use the embedded wave generation by Liam et al. (2014). Here we describe briefly the derivation of embedded wave generation with source function by Liam et al. (2014).

The first order translation or 1D uni-directional equation for positive traveling waves (toward positive x-axis) is

$$\partial_t \eta = -\mathcal{A}\eta$$

with

$$\mathcal{A}\eta = i \int \Omega(k)\hat{\eta}(k)e^{ikx}dk.$$

Here $\mathcal{A}$ is the (pseudo-differential) operator that has a connection with dispersion relation Ω and it is applied to function η in spectral space.

For shallow water, the dispersion relation is $\Omega(k) = C_0 k$ with $C_0 = \sqrt{gh_0}$ which corresponds to $\mathcal{A} = C_0\partial_x$ and the equation become $\partial_t\eta = -C_0\partial_x\eta$. This is the solution of the wave equation in Equation (2.6) that travel to positive x-direction.

The embedded wave generation is accomplished by adding source function $S(x,t)$ in the equation as

$$\partial_t\eta = -\mathcal{A}\eta + S(x,t).$$

Suppose we have influx signal $s(t)$ at $x = 0$. The source function $S(x,t)$ have to be determined so that the solution of η at $x = 0$ is equal to the given signal $s(t)$. Consider the source function has the form

$$S(x,t) = q(x)f(t)$$

The condition of this source function has been discussed in detail by Liam (2013). The condition is

$$\hat{q}(K(\omega))\check{f}(\omega) = \frac{1}{2\pi}V_g(K(\omega))\check{s}(\omega). \tag{2.21}$$

The hat and check notation represent a temporal Fourier transform in space and time, respectively. The notation V_g is the group velocity and $K(\omega) = \Omega^-1(\omega)$ is the inverse of dispersion relation function.

To satisfy the condition in Equation (2.21), the functions of q and f is not unique. In this project, only point generation that is used for influx problem simulation, i.e. a source that is concentrated at a certain point $x = x_0$. These point source generation can be obtained by choosing the function q as Dirac-delta function $\delta(x - x_0)$. Subsequently, the source condition become

$$\hat{\delta}(k)\check{f}(\omega) = \frac{1}{2\pi}V_g(K(\omega))\check{s}(\omega)$$
$$\check{f}(\omega) = V_g(K(\omega))\check{s}(\omega)$$

Notice that the function f is the convolution between the influx signal $s(t)$ and the inverse temporal Fourier transform of the group velocity $\omega \to V_g(K(\omega))$. A more general choice is by choosing spatial distributed source of function q. A Gauss shape function has been used by Wei et al. (1999).

However, the Hamiltonian wave model in Equation (2.2) is a multi-directional dispersive wave equation. In one horizontal dimension (1D), it produce waves travelling to positive x-direction and negative x-direction symmetrically therefore the source function $S(x,t)$ have to be doubled. Here, we only consider bi-directional elevation influxing since we have the input signal in surface elevation η. The bi-directional elevation influxing in Hamiltonian equation is given as

$$\begin{aligned}\partial_t\eta &= \delta_\phi\mathcal{H}(\eta,\phi) + 2S(x,t)\\ \partial_t\phi &= -\delta_\eta\mathcal{H}(\eta,\phi).\end{aligned}$$

It's also possible to have the uni-directional influxing in Hamiltonian equation. For mathematics point of view, it is sophisticated to produce uni-directional wave influxing. However, it's not necessary since the waves will be damped near the boundary.

Notice that the source function was derived based on linear theory. In order to generate high waves into the nonlinear wave model, nonlinear adjustment is needed. Otherwise, undesirable spurious modes will be generated. Dommermuth (2000), for nonlinear wave generation Liam et al. (2014) proposed the nonlinear adjustment in space from the influx position.

2.3 Numerical implementation

The Hamiltonian wave model will be solved numerically. In this section, numerical implementation for HOS method and VBM in one horizontal dimensional (1HD) will be described. We use pseudo spectral method to solve HOS method and finite element method to solve VBM.

2.3.1 Spatial discretization

Pseudo Spectral method

Suppose surface elevation η and velocity potential Φ can be represented in Fourier space as follow

$$\eta(x,t) = \int \hat{\eta}(k,t) e^{ikx} dk$$
$$\Phi(x,z,t) = \int \hat{\Phi}(k,t) \frac{\cosh\left(k(z+h)\right)}{\cosh\ (kh)} e^{ikx} dk$$

where the hat notation represents the spatial Fourier transform. Denote $\mathcal{F}$ and $\mathcal{F}^{-1}$ are the Fourier transform and inverse Fourier transform in space. Subsequently, the vertical velocity is

$$\frac{\partial \Phi}{\partial z}(x,0,t) = \mathcal{F}^{-1}\left[\hat{\Phi}(k) k \tanh(kh)\right].$$

Since velocity potential Φ has to satisfy the Laplace equation, therefore we can calculate the second derivative of Φ with respect to z by

$$\frac{\partial^2 \Phi}{\partial z^2}(x,0,t) = -\frac{\partial^2 \Phi}{\partial x^2} = \mathcal{F}^{-1}\left[\hat{\Phi}(k) k^2\right].$$

From these we can get formula for the derivative of the velocity potential at order m with respect to z as

$$\frac{\partial^n \Phi^{(m)}}{\partial z^n}(x,0,t) = \mathcal{F}^{-1}\left[\hat{\Phi}^{(m)} E_n\right]$$

where

$$E_n = \begin{cases} k^n & \text{for n is even,} \\ k^n \tanh(kh) & \text{for n is odd.} \end{cases}$$

Therefore, the velocity potential and vertical surface velocity at order m in Equation (2.12) and (2.13) can be calculated as

$$\Phi^{(m)} = -\sum_{n=0}^{m-1} \frac{\eta^n}{n!} \mathcal{F}^{-1}\left[\mathcal{F}\left[\Phi^{(m-n)}\right] E_n\right]$$

$$W^{(m)} = \sum_{n=0}^{m-1} \frac{\eta^n}{n!} \mathcal{F}^{-1}\left[\mathcal{F}\left[\Phi^{(m-n)}\right] E_{n+1}\right]$$

In the numerical implementation of pseudo spectral method, we solve the dynamic equations of HOS method into Fourier space. For instance, the HOS method second order is written in Fourier space as

$$\begin{aligned}
\partial_t \hat{\eta} &= \widehat{W^{(1)}} + \left(\widehat{W^{(2)}} - \widehat{\partial_x \phi\, \partial_x \eta}\right) \\
\partial_t \hat{\phi} &= -g\hat{\eta} + \frac{1}{2}\left(-\widehat{(\partial_x \phi)^2} + \widehat{W^{(1)} W^{(1)}}\right).
\end{aligned}$$

The nonlinear terms can be calculated by pseudo spectral procedure, i.e. the multiplication of nonlinear terms is done in real space and then convert it back to Fourier space. For example,

$$\begin{aligned}
\widehat{\partial_x \phi\, \partial_x \eta} &= \mathcal{F}\left[\mathcal{F}^{-1}\left[ik\hat{\phi}\right] \mathcal{F}^{-1}\left[ik\hat{\eta}\right]\right] \\
\widehat{(\partial_x \phi)^2} &= \mathcal{F}\left[\left(\mathcal{F}^{-1}\left[ik\hat{\phi}\right]\right)^2\right].
\end{aligned}$$

Finite Element method

The solutions are aproximated by superpositions of the basis functions as

$$\begin{aligned}
\eta(x,t) &\approx \sum_i \eta_i(t) T_i(x) = \bar{\eta}(t) \cdot T(x) \\
\phi(x,t) &\approx \sum_i \phi_i(t) T_i(x) = \bar{\phi}(t) \cdot T(x) \\
\psi(x,t) &\approx \sum_i \psi_i(t) T_i(x) = \bar{\psi}(t) \cdot T(x)
\end{aligned} \tag{2.22}$$

where $\bar{\eta}(t)$, $\bar{\phi}(t)$, $\bar{\psi}(t)$ and $T(x)$ are vector functions. Notice that the highest order of spatial derivatives in the Lagrangian of VBM are first order. Therefore piecewise linear spline basis function is chosen for FEM implementation. For 1D FEM, these basis function is given as

$$T_i(x) = \begin{cases} \frac{x - x_{i-1}}{x_i - x_{i-1}} & \text{, if} \quad x \in [x_{i-1}, x_i] \\ \frac{x_{i+1} - x}{x_{i+1} - x_i} & \text{, if} \quad x \in [x_i, x_{i+1}] \\ 0 & \text{, else} \end{cases}$$

Substitute the approximation in Equation (2.22) into the Equation (2.3) leads to the discretized version of Lagrangian :

$$\bar{\mathcal{L}}(\bar{\eta},\bar{\phi},\bar{\psi}) = \int_t \left[M\bar{\phi}\cdot\partial_t\bar{\eta} - \bar{\mathcal{H}}(\bar{\eta},\bar{\phi},\bar{\psi})\right] dt. \tag{2.23}$$

Here M is the mass matrix, with elements as follow

$$M_{i,j} = \int_x T_i T_j dx.$$

The discretized Hamiltonian of the linear VBM is

$$\bar{\mathcal{H}}_{VBM} \approx \frac{1}{2}gM\bar{\eta}\cdot\bar{\eta} + \frac{1}{2}S^{(h)}\bar{\phi}\cdot\bar{\phi} + S^{(\beta)}\bar{\phi}\cdot\bar{\psi} + \frac{1}{2}S^{(\alpha)}\bar{\psi}\cdot\bar{\psi} + \frac{1}{2}M^{(\gamma)}\bar{\psi}\cdot\bar{\psi}$$

where $S^{(h)}$ and $S^{(\alpha)}$ are the stiffness matrices with elements

$$S^{(h)}_{i,j} = \int_x hT'_iT'_jdx$$
$$S^{(\beta)}_{i,j} = \int_x \beta T'_iT'_jdx$$
$$S^{(\alpha)}_{i,j} = \int_x \alpha T'_iT'_jdx,$$

and the $M^{(\gamma)}$ has elements

$$M^{(\gamma)}_{i,j} = \int_x \gamma T_iT_jdx.$$

Taking first variations of Equation (2.23) with respect to η, ϕ and ψ result the system equations in matrix system

$$M\partial_t\bar{\eta} = S^{(h)}\bar{\phi} + S^{(\beta)}\bar{\psi}$$
$$M\partial_t\bar{\phi} = -gM\bar{\eta}$$
$$S^{(\alpha)}\bar{\psi} + M^{(\gamma)}\bar{\psi} = S^{(\beta)}\bar{\phi}.$$

2.3.2 Initialization and time stepping

For the initial value problem, the prescribed surface elevation η and velocity potential ϕ have to be periodic in HOS method because of the natural boundary condition of the pseudo spectral method. On the other hand, there is no requirement for the VBM since the natural boundary condition of FEM is hardwall.

For the influx problem, embedded wave generation is implemented with nonlinear adjustment as described in Liam et al. (2014) The initial condition for both η and ϕ is set to be zero.

For the time integration, we use ODE solver from MATLAB which has adaptive time step. There are several ODE solvers from MATLAB, e.g. ode45, ode113, and ode23. Here we use ode23 that is an implementation of an explicit Runge-Kutta (2,3) pair of Bogacki and Shampine (1989).

The shortest wave component should be represented by enough grid points, let say one wave is well defined by at least 10 grid points. This shortest wave component leads to a largest wave number k_{max} and will be the cut-off for the filtering. In fully nonlinear VBM, aliasing error is prevented by filtering the output after each 50 or 100 time steps. Meanwhile in HOS method the filtering is done by setting the higher modes larger than k_{max} to be zero in each time step.

2.3.3 Nonlinear adjustment and damping zones

Nonlinear adjustment is implemented as described in Liam et al. (2014), we separate the linear and nonlinear terms and multiply the nonlinear terms with a characteristic smooth function χ_{nonlin}.

The pseudo spectral method leads to a periodic solution, i.e. the solution in right boundary is equal to solution in left boundary or in other words the waves propagate to the right boundary will be forwarded to the left boundary. On other hand, the natural boundary conditions for finite element method is hardwall. In the influxing problem, we add energy into the domain. It means the propagating waves toward the boundaries have to be vanished. Instead of modifying the boundary conditions to be transparent, we use damping zones so that the wave will be vanished smoothly near the boundaries. Therefore, we define another characteristic smooth function $\chi_{damping}$ which has value one in the boundaries and vanished towards the inside of domain.

The dynamic equations with nonlinear wave generation and damping zones is

$$\partial_t \eta = RHS_{lin} + \chi_{nonlin} RHS_{nonlin} - \chi_{damping} \eta$$
$$\partial_t \phi = RHS_{lin} + \chi_{nonlin} RHS_{nonlin} - \chi_{damping} \phi.$$

An illustration of the characteristic functions for nonlinear adjustment and damping zones are shown in Figure 2.1. Normally, the length of damping zones are larger than two times of peak wave length.

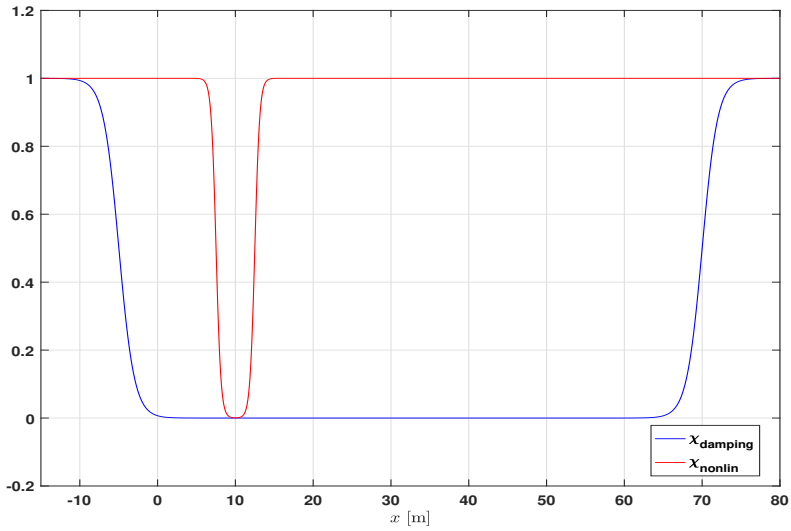

Figure 2.1: Characteristic smooth functions for damping zones (blue, solid) and nonlinear adjustment (red, solid) with influx position at $x = 10$ m.

Chapter 3

Higher Order Spectral Method on Variable Depth

The Higher order spectral (HOS) method was first developed by Dommermuth and Yue (1987) and West et al. (1987) for flat bottom. Later, Liu and Yue (1998) introduced an additional velocity potential to deal with varying bottom. However, this method uses the same order of non-linearity for the bottom and the free surface. In order to give more flexibility in order of non-linearity, Gouin et al. (2016) adapted the work of Guyenne and Nicholls (2007) from Dirichlet to Neumann (DtN) model to the HOS method by considering two independent orders of non-linearity.

van Groesen and Andonowati (2011) derive fully dispersive models for varying bottom, so-called AB model. In van Groesen and van der Kroon (2012), hybrid spatial spectral implementation was used in AB model. Multiple works in Kurnia and van Groesen (2014), van Groesen et al. (2017), van Groesen and Wijaya (2017) are based on this method. This method will be adapted into HOS method and is referred as hybrid spatial spectral method in this thesis.

In this chapter, two methods to deal with varying bottom which were proposed by Gouin et al. (2016) and van Groesen and Andonowati (2011) will be discussed. The former is referred as original method while the latter is referred as hybrid spatial spectral method.

3.1 Original method

Let $z = \eta(x,t)$ represents the free surface elevation, h is the total water depth, h_0 is mean depth, and $\xi(x)$ is the bottom variation, such as $-h(x) = -h_0 + \xi(x)$. In HOS method,

the free surface boundary condition is

$$\begin{aligned}\frac{\partial \eta}{\partial t} &= W(1+\left|\frac{\partial \eta}{\partial x}\right|^2) - \frac{\partial \eta}{\partial x}\cdot\frac{\partial \phi}{\partial x} \\ \frac{\partial \phi}{\partial t} &= -g\eta - \frac{1}{2}\left|\frac{\partial \phi}{\partial x}\right|^2 + \frac{1}{2}W^2(1+\left|\frac{\partial \eta}{\partial x}\right|^2).\end{aligned}$$

HOS method only needs to evaluate the vertical velocity at free surface $W(x,t) = \frac{\partial \Phi}{\partial z}(x, z = \eta, t)$ for the time evolution of free surface elevation η and surface potential ϕ. This quantity W is essential in HOS method and it is affected by the bathymetry. For uneven bottom, the bottom boundary condition is

$$\frac{\partial \Phi}{\partial x}\frac{\partial \xi}{\partial x} - \frac{\partial \Phi}{\partial z} = 0 \quad \text{on} \quad z = -h_0 + \xi(x).$$

Liu and Yue (1998) introduce an additional potential to deal with varying bathymetry. The total potential Φ is expressed as

$$\Phi_{total} = \Phi_{h_0} + \Phi_{\xi}.$$

Φ_{h_0} satisfies a Neumann condition on $z = -h_0$, therefore Φ_{h_0} is the solution of the Laplace problem at constant depth h_0 :

$$\frac{\partial \Phi_{h_0}}{\partial z}(x, -h_0, t) = 0 \quad \text{on} \quad z = 0.$$

Φ_{ξ} is added for the remedy of bottom boundary condition and satisfies a Dirichlet condition on $z = 0$:

$$\Phi_{\xi}(x, 0, t) = 0 \quad \text{on} \quad z = 0.$$

Furthermore, the potentials are expressed in Fourier space taking into account the previous boundary conditions as :

$$\begin{aligned}\Phi_{h_0}(x,z,t) &= \int \widehat{\Phi_{h_0}}(k,t)\frac{\cosh\left(k(z+h_0)\right)}{\cosh\ (kh_0)}e^{ikx}dk \\ \Phi_{\xi}(x,z,t) &= \int \widehat{\Phi_{\xi}}(k,t)\frac{\sinh\left(kz\right)}{\cosh\ (kh_0)}e^{ikx}dk.\end{aligned}$$

In HOS method, the total potential is represented as a truncated power series of order M (M is the order of nonlinearity of the HOS method). Liu and Yue (1998) truncated the bottom condition also at order M. Meanwhile, Gouin et al. (2016) adapted the method from Dirichlet to Neumann (DtN) modeling by Craig et al. (2005) and Guyenne and Nicholls (2007) by Taylor expansion of the bottom boundary conditions with a different order of

truncation M_b :

$$\begin{aligned}\sum_{m=1}^{M}\Bigg[&\left(\frac{\partial\Phi_{total}^{(m)}}{\partial x}\frac{\partial\xi}{\partial x}\right)_{-h_0}+\xi\frac{\partial}{\partial z}\left(\frac{\partial\Phi_{total}^{(m)}}{\partial x}\frac{\partial\xi}{\partial x}\right)_{-h_0}\\&+\cdots+\frac{\xi^{M_b-1}}{(M_b-1)!}\frac{\partial^{M_b-1}}{\partial z^{M_b-1}}\left(\frac{\partial\Phi_{total}^{(m)}}{\partial x}\frac{\partial\xi}{\partial x}\right)_{-h_0}\Bigg]\\=\sum_{m=1}^{M}\Bigg[&\left(\frac{\partial\Phi_{total}^{(m)}}{\partial x}\right)_{-h_0}-\xi\left(\frac{\partial^2\Phi_{total}^{(m)}}{\partial x^2}\frac{\partial\xi}{\partial x}\right)_{-h_0}\\&-\cdots-\frac{\xi^{M_b}}{(M_b)!}\frac{\partial^{M_b-1}}{\partial z^{M_b-1}}\left(\frac{\partial^2\Phi_{total}^{(m)}}{\partial x^2}\right)_{-h_0}\Bigg].\end{aligned}\tag{3.1}$$

Equation (3.1) is truncated consistently by expanding the left hand side up to order M_b-1 since $O(\xi)\equiv O\left(\frac{\partial\xi}{\partial x}\right)$. Additionally, it is assumed that each potential $\Phi_\xi^{(m)}$ as a truncated power series up to order M_b (M_b is the order of nonlinearity of the bottom):

$$\Phi_\xi^{(m)}=\sum_{l=1}^{M_b}\Phi_\xi^{(m,l)}.$$

At each order m, the total potential is $\Phi_{total}^{(m)}=\Phi_{h_0}^{(m)}+\Phi_\xi^{(m)}$. By keeping only the terms of maximum order $m+M_b$ and assuming $O(\xi)\equiv O\left(\frac{\partial\xi}{\partial x}\right)\equiv O(\eta)$, Equation (3.1) become:

$$\begin{aligned}\left(\frac{\partial\Phi_\xi^{(m)}}{\partial z}\right)_{-h_0}=&\sum_{l=1}^{M_b}\left(\frac{\partial\Phi_\xi^{(m,l)}}{\partial z}\right)_{-h_0}\\=&\sum_{l=1}^{M_b}\left\{\frac{\partial}{\partial x}\frac{\xi^l}{l!}\left[\frac{\partial^{l-1}}{\partial z^{l-1}}\left(\frac{\partial\Phi_{h_0}^{(m)}}{\partial x}\right)\right]_{-h_0}\right\}\\&+\sum_{l=1}^{M_b}\sum_{p=1}^{l-1}\left\{\frac{\partial}{\partial x}\frac{\xi^p}{p!}\left[\frac{\partial^{p-1}}{\partial z^{p-1}}\left(\frac{\partial\Phi_\xi^{(m,l-p)}}{\partial x}\right)\right]_{-h_0}\right\}.\end{aligned}$$

Subsequently, the fourier amplitude $\widehat{\Phi_\xi}$ can be calculated iteratively at a given order m. The explicit expression for this formulas can be found in Gouin et al. (2016).

3.2 Hybrid spatial spectral method

van Groesen and Andonowati (2011) showed that the kinetic energy can be written with a positive definite symmetric operator C as

$$\mathcal{K}=\frac{1}{2g}\int C^2\left(\partial_x\phi\right)^2dx\tag{3.2}$$

where C is phase velocity operator. For flat bottom, $C = \sqrt{g \tanh kh/k}$ is pseudo-differential operator (PDO) where h is constant depth and k is the wavenumber. To deal with varying bottom, the variable $h(x)$ is included in the phase velocity. Therefore it is not a PDO anymore but it is called Fourier integral operator (FIO), an extension of the class of PDO's. It is computationally expensive to calculate the FIO because a Fast-Fourier Transform (FFT) is required for each spatial grid. However, the computational time can be reduced significantly by using a piecewise constant approximation or by interpolation method. Kurnia and van Groesen (2017) showed that the second order accurate wave model over varying bottom can be derived by introducing the nonlinear phase velocity operator

$$C = \sqrt{\frac{g \tanh k\left(h(x) + \eta(x,t)\right)}{k}}.$$

As in van Groesen and van der Kroon (2012), a hybrid spatial spectral method to approximate the FIO $C^2(k, h(x))$ is described briefly in the following. The FIO $C^2(k, h(x))$ is approximated by using a suitable smooth interpolation between the squared phase velocity at the deepest part (h_0) and the shallowest part (h_1),

$$C^2_{approx}\left(k, h(x)\right) = a(x)C^2(k, h_0) + b(x)C^2(k, h_1).$$

Let ν be a characteristic peak frequency, then $\kappa(x)$ is the wave number corresponding to ν at depth x, $\Omega(\kappa(x), h) = \nu$, where Ω is the function describing the dispersion relation. The coefficients $a(x)$ and $b(x)$ can be determined uniquely by having two conditions. First, the squared phase velocity is required to has the exact value for all these wave numbers:

$$C^2\left(k, h(x)\right) = a(x)C^2\left(\kappa(x), h_0\right) + b(x)C^2\left(\kappa(x), h_1\right).$$

Secondly, the frequency also has to be exact for these wave numbers:

$$\nu = a(x)\Omega\left(\kappa(x), h_0\right) + b(x)\Omega\left(\kappa(x), h_1\right).$$

3.2.1 Limiting cases

In this subsection, two limiting cases which are shallow water and Airy's linear wave theory are given to show that the wave equation can be derived through approximation of kinetic energy in Equation (3.2).

Shallow water

For shallow water condition, the horizontal velocity is assumed uniform from the bottom until free surface. Therefore it is natural to approximate the velocity potential by $\Phi(x, z, t) = \phi(x, t)$. Then

$$\mathcal{K}_{SW} = \frac{1}{2}\int (h + \eta)(\partial_x \phi)^2 dx.$$

Notice that $\mathcal{K}_{SW}$ can be expressed as in Equation (3.2) with $C = \sqrt{g(h + \eta)}$ is the nonlinear phase velocity for shallow water.

Airy's linear wave theory

The solution of the Laplace equation above flat bottom with depth h is

$$\Phi(x,z,t) = \int \hat{\phi}(k,t)\frac{\cosh\, k(z+h)}{\cosh\, kh}e^{ikx}dk.$$

And also the well known linear dispersion relation is

$$C_0 = \frac{\omega}{k} = \sqrt{\frac{g\,\tanh\, kh}{k}}. \tag{3.3}$$

From the wave equation and using the linear phase velocity C_0 in Equation (3.3), the equations for linear waves above flat bottom are given by

$$\begin{aligned} \partial_t\eta &= -\frac{1}{g}\partial_x\left(C_0^2\partial_x\phi\right) \\ \partial_t\phi &= -g\eta. \end{aligned} \tag{3.4}$$

Observe that Equation (3.4) can also be derived from the Hamiltonian with kinetic energy as follow

$$\mathcal{K}_0 = \frac{1}{2g}\int (C_0\partial_x\phi)^2 dx. \tag{3.5}$$

3.2.2 HOS method with hybrid spatial spectral method

As discussed in Chapter 2.1.2, the vertical velocity is calculated recursively. In the HOS method implementation for flat bottom, the derivative of velocity potential with respect to z is pseudo-differential operator. In order to deal with uneven bottom, this operator will become Fourier integral operator (FIO) and the formulation of this FIO will be discussed in the following.

From Equation (3.4), the linear vertical velocity at the surface can be expressed as

$$W^{(1)} = -\frac{1}{g}\partial_x C_0^2\partial_x\phi = L\phi \tag{3.6}$$

where operator L is defined as the derivative with respect to z. This operator L will replace operator E and will be exactly the same with operator E for flat bottom. For varying bottom, the phase velocity operator C_0^2 is Fourier integral operator and is implemented by using hybrid spatial spectral method as described above.

This operator L can also be obtained by using quasi homogeneous approximation. During propagation above varying bottom, the dispersive properties change since the dispersion relation depends on depth. In quasi homogeneous approximation, the wave properties are determined by the local dispersion relation. Therefore, at each position x the fluid domain is replaced by horizontal strip with constant depth $h(x)$.

In the following, the operator L in equation (3.6) will be achieved from quasi homogeneous way. The velocity potential is represented in Fourier space as

$$\Phi(x,z) = \int \hat{\Phi}(k)\frac{\cosh\left(k(z+h(x))\right)}{\cosh\ \left(kh(x)\right)}e^{ikx}dk. \tag{3.7}$$

Then the linear vertical velocity is

$$\begin{aligned}
\partial_z \Phi(x,0) &= \int \hat{\Phi}(k)\ k\ \tanh\left(kh(x)\right) e^{ikx} dk \\
&= -\frac{1}{g} \int ik\hat{\phi}(k)\ \frac{g\ \tanh\left(kh(x)\right)}{k} ik\ e^{ikx} dk \\
&= -\frac{1}{g} \int ik\hat{\phi}(k)\ C_0^2\ ik\ e^{ikx} dk \\
&= -\frac{1}{g} \partial_x C_0^2 \partial_x \phi.
\end{aligned} \tag{3.8}$$

Chapter 4

Numerical Investigation

Dispersion and nonlinearity quality of the HOS method are investigated in this chapter. Furthermore, the method that has been discussed in previous chapter will be tested and utilized. In the first subsection, solitary wave propagation over flat bottom case is considered. In the following three subsections, the HOS method is tested against wave tank experiment, namely bichromatic wave train experiment, focusing wave group experiment, regular and irregular waves over a submerged bar. In the last subsection, irregular waves over a sloping bottom is investigated to study the behaviour of rogue wave occurence over non-uniform bathymetry.

4.1 Solitary wave propagation over flat bottom

The first test case is solitary wave propagation over a constant depth. In order to maintain the shape of the solitary wave, the wave model needs a good dispersion and nonlinearity properties. Dutykh and Clamond (2014) provide solitary wave solutions for free surface Euler equations which is computed numerically. In this numerical experiment, we choose the initial condition by Dutykh and Clamond (2014) with high nonlinearity which has amplitude 0.7 m and water depth 1 m. Figure 4.1 show the initial condition for free surface η and velocity potential ϕ.

Lawrence et al. (2018) has shown that the fully nonlinear VBM retains both shape and speed of the Euler soliton. Here we choose fully nonlinear VBM as a reference solution for testing the convergence of the HOS nonlinearity. In Figure 4.2, we show the simulation results for HOS method up to 7th order compared to FN-VBM. Quantitative informations for the HOS method compared to FN-VBM are given in terms of correlation and variance-quotient in Table 4.1. These quantities are calculated in interval $x = (70; 90)$ m at $t = 20$ s. The simulation results indicate that the HOS method converge to fully nonlinear model by increasing the nonlinear order.

In Figure 4.3, interesting phenomena is observed for longer time simulation. For HOS third order, it retain the solitary wave shape with lower wave height after shedding off

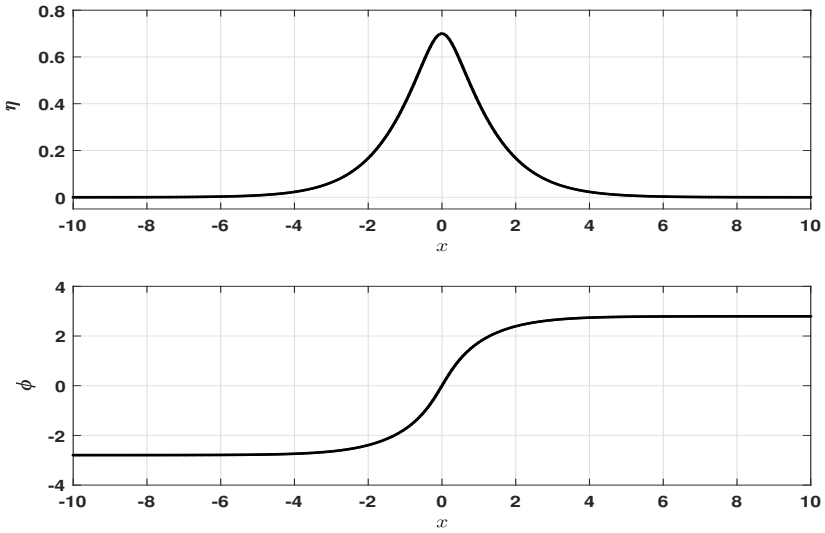

Figure 4.1: The initial wave elevation (upper plot) and velocity potential (lower plot) of the solitary wave with height of 0.7 m.

Table 4.1: Comparison of correlation and variance-quotient for HOS method up to 7th order in solitary wave propagation case.

	Correlation	Variance-quotient
HOS 3rd	0.9290	0.9930
HOS 4th	0.8993	1.0039
HOS 5th	0.9970	0.9988
HOS 6th	0.9993	1.0009
HOS 7th	1.0000	1.0002

some slower waves. This result confirm the work by Lawrence et al. (2018) that Hamiltonian wave possess the steady waves propagation even with low order approximation in Hamiltonian. This also prove that the HOS method is energy conserved which is one of the properties of Hamiltonian wave model.

4.2 Bichromatic wave train experiment

Two experiments with bichromatic waves (Test 60 and Test 61) were conducted in the 270 m long and 1 m wide wave tank at MARINTEK, Trondheim, Norway. A hydraulic-drive double flap wave maker was installed at one end of the tank and at the other end waves are absorbed by a sloping beach. The still water depth is 10 m in the range 0-80 m from the wave maker and 5 m elsewhere. The wave elevation was measured at 6 different locations

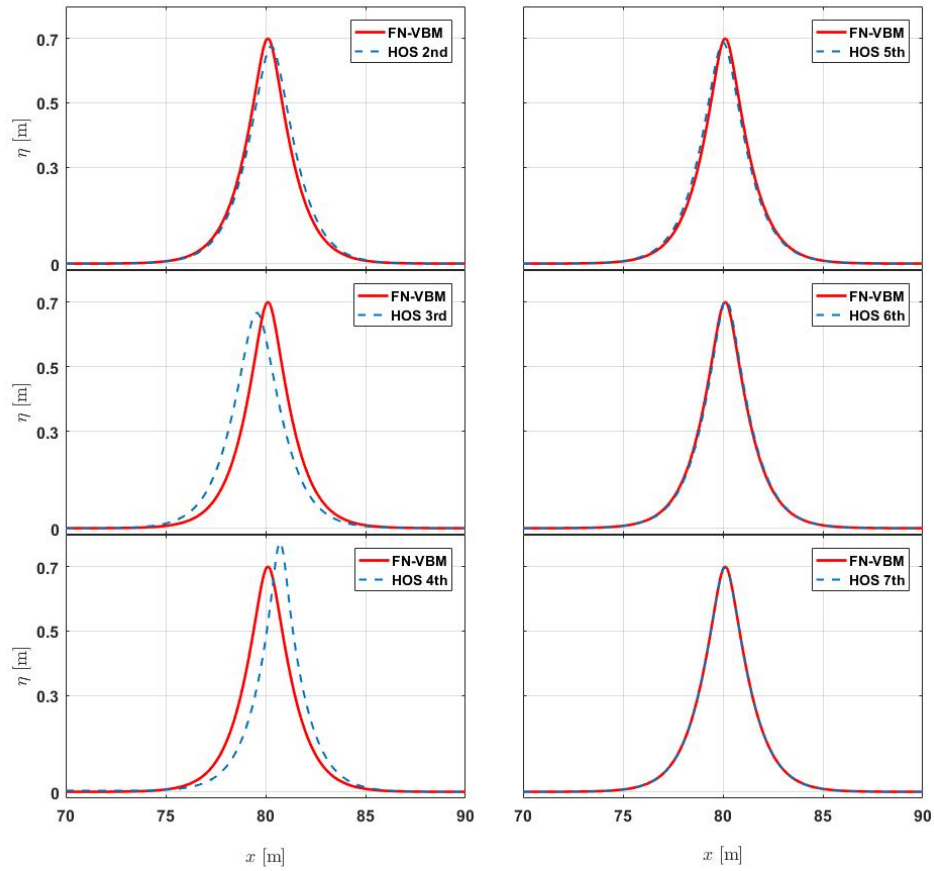

Figure 4.2: Comparison for solitary wave simulation between FN-VBM (blue, dash) and HOS up to 7th order (red, solid) at t = 20 s.

: W1 at $x = 9.3$ m, W2 at $x = 40$ m, W3 at $x = 80$ m, W4 at $x = 120$ m, W5 at $x = 160$ m, and W6 at $x = 200$ m. The layout of the experimental setup is shown in Figure 4.4 . Further details of the experiment are reported in Stansberg (1998). The specification of these two experiments is described in table below. In this project report, we only focus on Test 60.

Table 4.2: Wave properties for bichromatic wave train experiment

Test	Wave periods		Wave heights	
	T_1 [s]	T_2 [s]	H_1 [m]	H_2 [m]
60	1.90	2.10	0.16	0.16
61	0.95	1.05	0.04	0.04

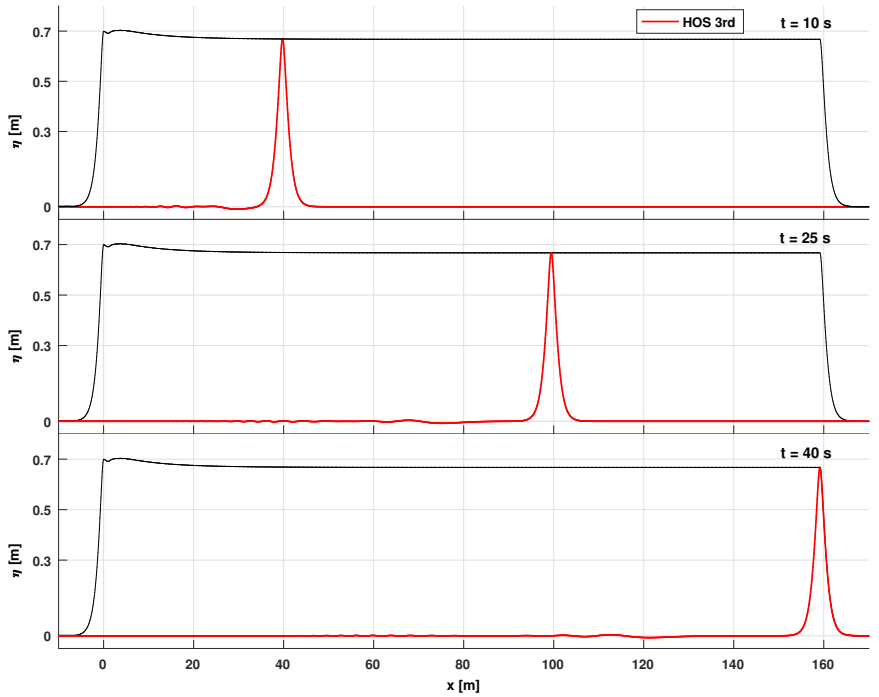

Figure 4.3: Simulation results of the HOS third order (red, solid) and the Maximum Temporal Crest (black, solid) at t = 10, 25, 40 s.

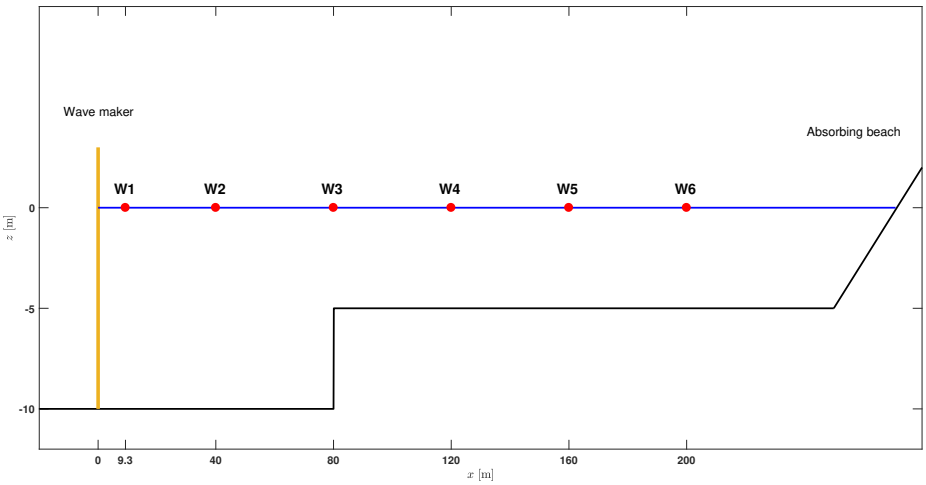

Figure 4.4: Sketch of the wave tank with the location of wave gauges.

The nondimensional depth $kh_0 = 10$ for the first 80 m and $kh_0 = 5$ for the rest of the wave tank. Here we present the HOS simulation with $kh_0 = 10$ for the whole domain. As discussed in Trulsen and Stansberg (2001), the effect of the jump at 80 m is not important. The measurement at first wave gauge W1 is used as an influx signal for the simulation.

Neither HOS first order nor HOS second order predict the wave elevation correctly. The simulation result for HOS first and second order are given in Appendix, meanwhile for the HOS third order is shown in Figure 4.5, 4.6, 4.7, 4.8, and 4.9. As expected by linear theory, there is no energy transfer between free modes and it retain the shape of bichromatic wave group. For the second order effect, it can be sum or difference of the frequency. Suppose the bichromatic wave travel with frequency ω_1 and ω_2 with $\omega_2 > \omega_1$ and denote $\Delta\omega = \omega_2 - \omega_1$. The higher order modes $2\omega_1$ and $2\omega_2$ are generated by sum frequency of ω_1 and ω_2, respectively. This modes is called the bound waves. These $2\omega_1$ mode can interact with ω_2 mode and generate the first left side band mode, i.e. the mode with frequency $\omega_1 - \Delta\omega$. In a similar way, the first right band side mode ($\omega_2 + \Delta\omega$ mode) is generated by $2\omega_2$ mode and ω_1 mode. In the HOS second order simulation, it is observed that the side band modes are generated. However, the energy transfer is very weak because it's generated from the higher order mode $2\omega_1$ and $2\omega_2$ which have small energy. For this experiment, third order effects need to be take into account since the side band modes is generated from the free modes ω_1 and ω_2 directly. For instance, the first right side band frequency is generated by $\omega_2 + \Delta\omega = \omega_2 + \omega_2 - \omega_1$. From this, the side band modes are grow automatically from the free modes ω_1 and ω_2 contribution. Therefore the third order effects is important in this experiment.

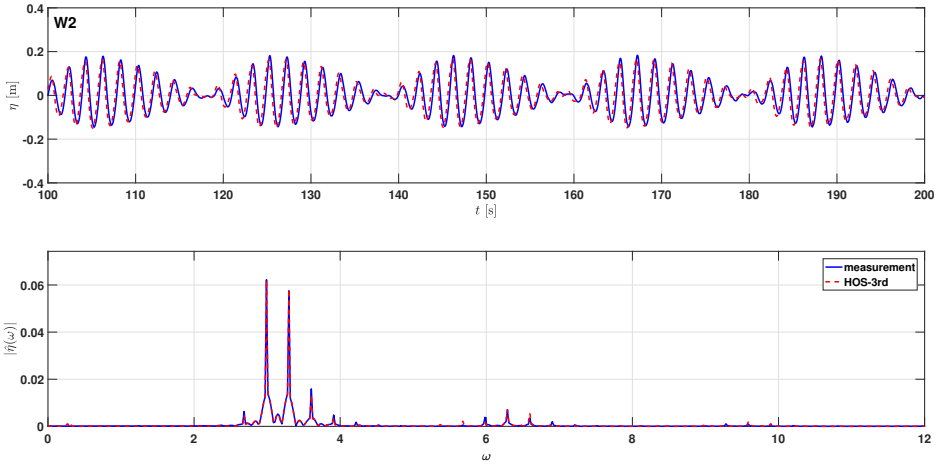

Figure 4.5: Comparison of wave elevation (upper plot) and amplitude spectrum (lower plot) for bichromatic wave train experiment between HOS third order (red, dash) and measurement (blue,solid) at position W2 ($x = 40$ m).

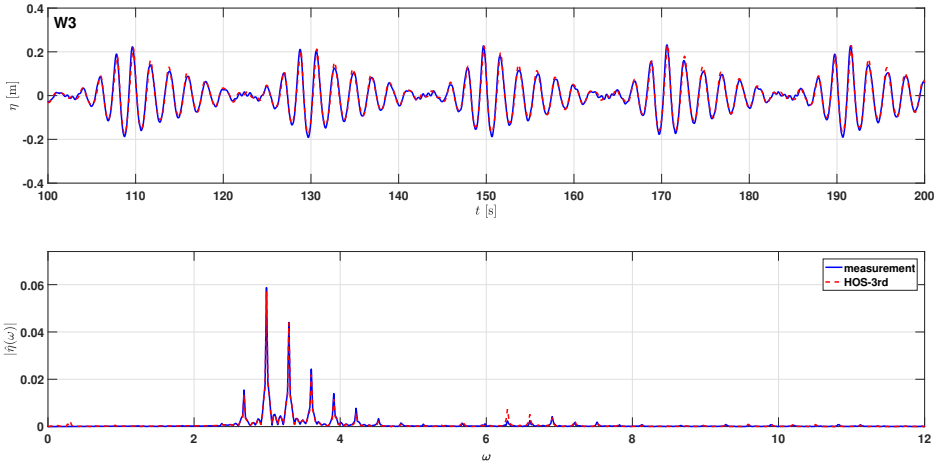

Figure 4.6: Same as Figure 4.5. Now at position W3 ($x = 80$ m).

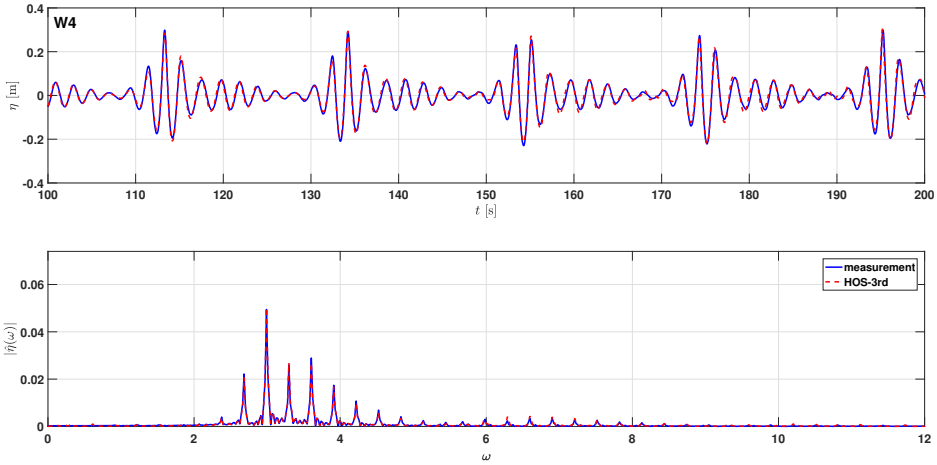

Figure 4.7: Same as Figure 4.5. Now at position W4 ($x = 120$ m).

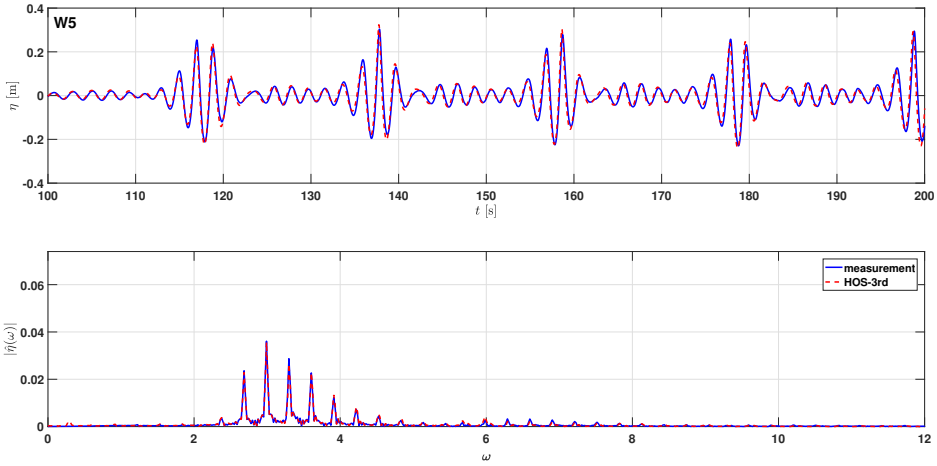

Figure 4.8: Same as Figure 4.5. Now at position W5 ($x = 160$ m).

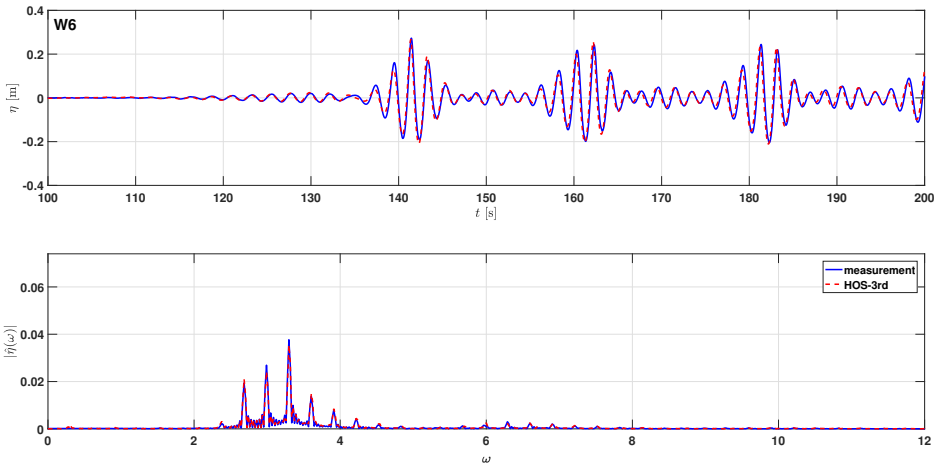

Figure 4.9: Same as Figure 4.5. Now at position W6 ($x = 200$ m).

In Table 4.3, we present the correlation and variance quotient for 300 s simulation at different measurement locations. We observe that simulation of HOS third order gives correlation over than 0.85 and variance quotient error less than 0.03 which show energy conservation property of the hamiltonian wave model.

Table 4.3: Correlation and Variance-quotient for HOS third order simulation in bichromatic wave experiment.

Position	Correlation	Variance-quotient
W2	0.854	0.996
W3	0.987	0.972
W4	0.981	0.993
W5	0.926	0.995
W6	0.893	0.982

4.3 Focusing wave group experiment

The focusing wave group experiment (MARIN 101013) was conducted in 200 m long wave tank with 1 m water depth at Maritime Research Institute of Netherlands (MARIN), Wageningen, Netherlands. The experiment is designed to have a focused wave at certain position by generating first short period small amplitude waves, followed by longer and higher waves. The wave was generated by flap wave maker at position $x = 0$, and was measured at $x_0 = 10$ m and $x_1 = 50$ m. The experiment was designed to have a focused wave at position $x = 50$ m. The measured elevation at $x_0 = 10$ m is used as influx signal for the simulation. The influx signal and the amplitude spectrum are shown in Figure 4.10. The measurement of the elevation at x_1 is the only available data around the focusing position. As seen in Figure 4.10, this dispersive focusing experiment requires a

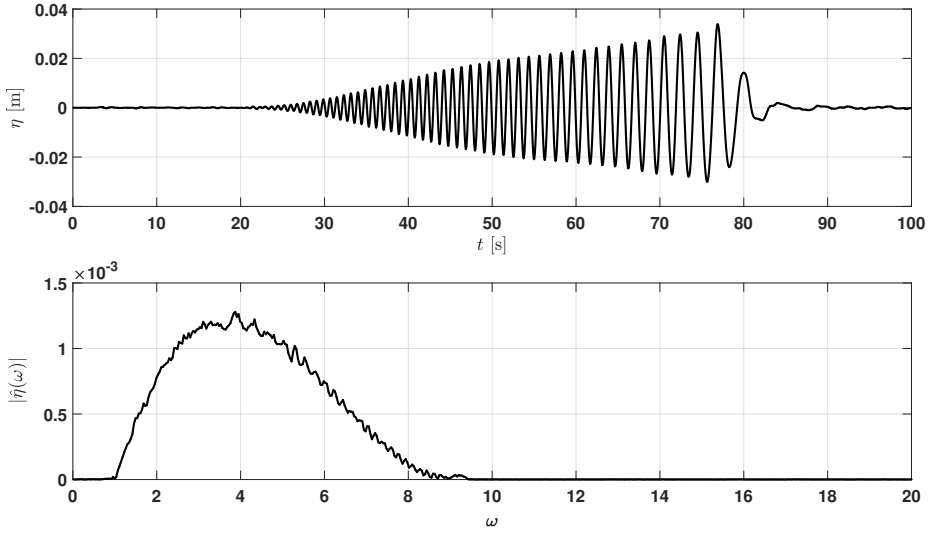

Figure 4.10: The influx signal (upper plot) and the amplitude spectrum (lower plot) of the focusing wave group experiment

broad spectrum, therefore the dispersion of the wave model plays an important role in this

experiment. In the experiment, some breaking wave (white capping) was observed just downstream of the focusing point which means the nonlinearity is also important.

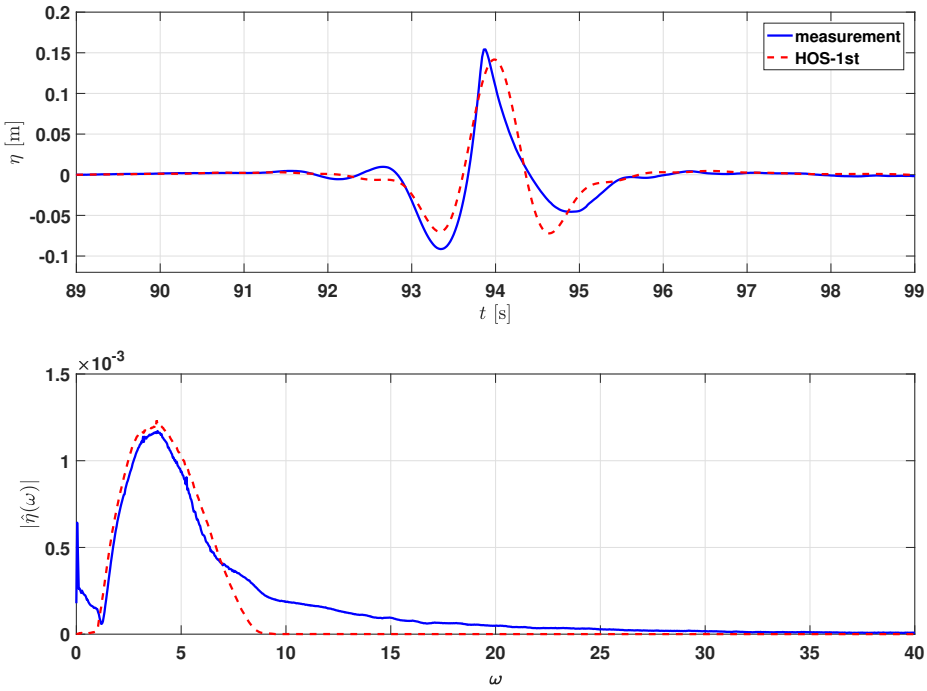

Figure 4.11: Comparison of wave elevation (upper plot) and amplitude spectrum (lower plot) for focusing wave group experiment between HOS first order (red, dash) and measurement (blue, solid) at $x = 50$ m.

The simulation result for HOS first order is shown in Figure 4.11. As expected, there is no energy transfer between fourier mode as seen in the amplitude spectrum plot. In reality, the spectrum will deform from the initial spectrum and the energy in spectrum tail will be increased due to nonlinear interaction. In Figure 4.12, the deformation in spectrum tail is well predicted by HOS third order simulation . However, the wave propagates too fast since the correct profile is observed 0.2 m further as shown in Figure A.11 in Appendix. The difference between linear and nonlinear simulation can be observed in Figure 4.13. The linear simulation predict the focused point exactly at $x = 50$ m as initial design of the experiment. Due to the nonlinearity, the focused point is shifted more than 1 m and the resulting wave profile for nonlinear simulation at focused point is steeper than the linear simulation.

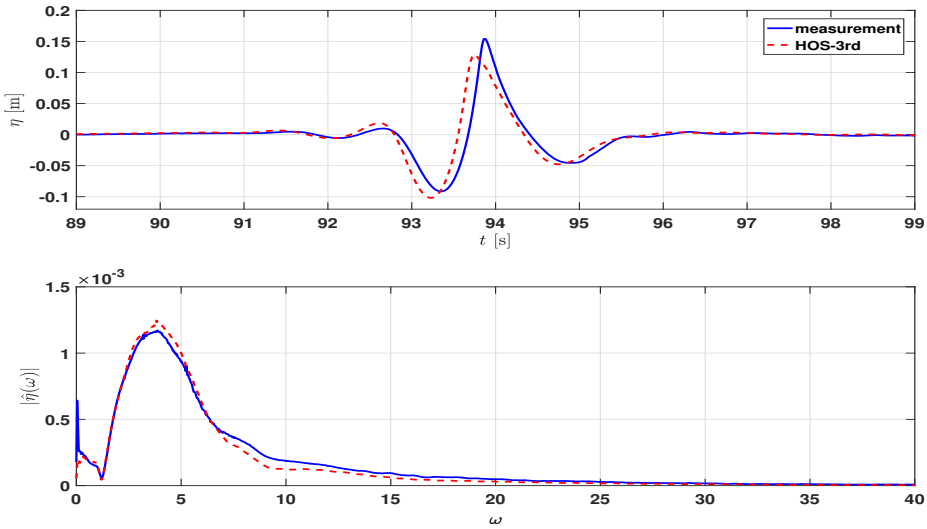

Figure 4.12: Comparison of wave elevation (upper plot) and amplitude spectrum (lower plot) for focusing wave group experiment between HOS third order (red, dash) and measurement (blue, solid) at $x = 50$ m.

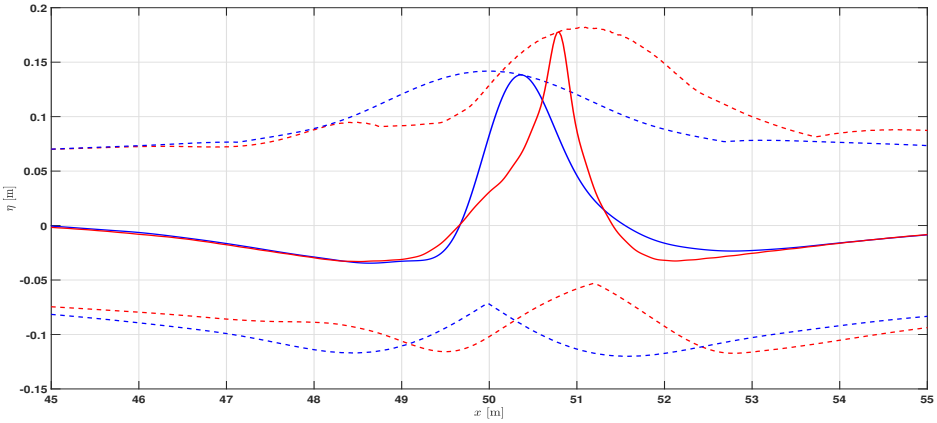

Figure 4.13: Spatial wave profiles for HOS first order (blue, solid), and for HOS third order (red, solid) at time t = 94.2 s and the Maximum Temporal Amplitudes for HOS first order (blue, dash) and HOS third order (red, dash).

4.4 Regular and irregular waves over a submerged bar

Wave propagation over a submerged bar is a suitable test to check the nonlinearity and dispersion of a wave model. On the front slope of a bar, higher harmonic bound waves are

generated and the waves become higher and steeper, i.e. the wavelength become shorter. The bound waves become free on top of the bar while on the back slope the wave energy is transferred back to lower harmonics.

Beji and Battjes (1993) conducted a series of experiments concerning the propagation of regular and irregular waves over a submerged bar with non-breaking or breaking waves. In this thesis, only non-breaking case for both regular and irregular waves is considered. The bathymetry is shown in Figure 4.14 which has 1:20 front slope followed by 2 m flat bottom and a 1:10 back slope. The water depth varies from 0.4 m in the deeper region to 0.1 m on top of the bar. In the experiment the wave elevation is measured at seven positions: $W1 = 5.7$ m, $W2 = 10.5$ m, $W3 = 12.5$ m, $W4 = 13.5$ m, $W5 = 14.5$ m, $W6 = 15.7$ m, $W7 = 17.3$ m. The regular (harmonic) case has wave period $T = 2$ s and wave height $H = 2$cm. Meanwhile the irregular case has a JONSWAP-type spectrum with peak period $T_p = 2$ s and significant wave height $H_s = 1.8$ cm.

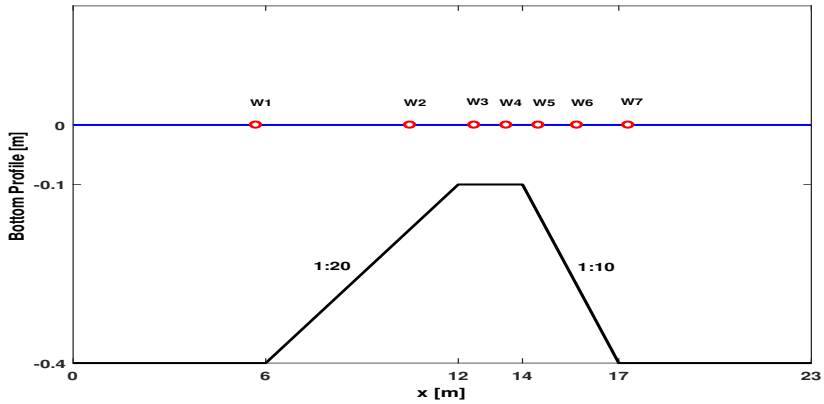

Figure 4.14: Bottom profile of the experiment of Beji and Battjes (1993).

To perform simulations for these cases, second order HOS method with 2^{11} grid points are used for both original and hybrid spatial spectral method. Evolution of surface elevation from the simulation using hybrid spatial spectral method are shown in Figure 4.15 for regular waves and in Appendix for irregular waves. In Table 4.4 and 4.5, statistical properties (correlation and variance quotient) and relative computation time (C_{rel}) are given for irregular wave case. The relative computation time is defined as the cpu-time divided by the total time of the simulation. The simulations were performed on a laptop with CPU i7, 2.50 GHz processor with 16 GB memory. The original method with third order nonlinearity for the bottom (Mb=3) give poorer result in correlation compared to the other method. However, it can be improved by increasing the nonlinearity order, in this case Mb=5 is used. On the other hand, the computational time is more expensive by increasing the nonlinear order for the bottom in original method. The hybrid spatial spectral method gives better computational time due to efficiency and consistency in solving the dynamic equation only at the surface. Overall, the second order simulation give satisfactory results compared to experimental data.

Table 4.4: Statistical properties and computational relative time for irregular waves over submerged bar simulation using Original method with $M_b = 3$ and $M_b = 5$.

	Original Method (Mb=3)		**Original Method (Mb=5)**	
C_{rel}	0.31		0.75	
Position	**Correlation**	**Variance-Quotient**	**Correlation**	**Variance-Quotient**
W2	0.976	1.001	0.979	1.005
W3	0.943	0.995	0.967	1.012
W4	0.923	0.986	0.972	1.009
W5	0.833	1.027	0.950	1.033
W6	0.853	1.038	0.961	1.023
W7	0.860	1.043	0.963	1.029

Table 4.5: Statistical properties and computational relative time for irregular waves over submerged bar simulation using Hybrid spatial spectral method.

	Hybrid Spatial Spectral Method	
C_{rel}	0.18	
Position	**Correlation**	**Variance-Quotient**
W2	0.960	1.006
W3	0.953	1.024
W4	0.966	1.029
W5	0.922	1.065
W6	0.950	1.048
W7	0.952	1.067

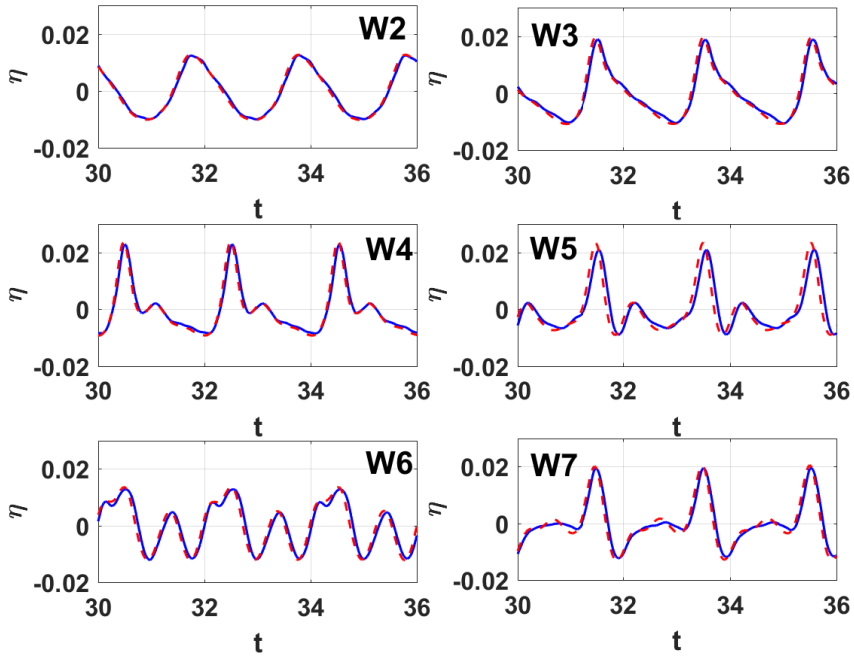

Figure 4.15: Comparison for harmonic wave over a submerged bar experiment between second order HOS method with hybrid spatial spectral method (red, dashed) and measurement (blue, solid).

4.5 Irregular waves over a sloping bottom

The propagation of waves from deep water towards shallow water may enhance the occurence of rogue waves. Sergeeva et al. (2011) used a Korteweg-de Vries (KdV) model to observe that there is a local maximum of kurtosis near the shallower edge of slope. In their simulation, the waves propagate from $kh = 0.44$ to $kh = 0.3$. Zeng and Trulsen (2012) studied in deeper water depth by utilizing the Nonlinear schrodinger equation (NLS). It is found that the skewness and kurtosis are decreasing in the shallower region with assumption the wavelength is shorter than the slope length. In Trulsen et al. (2012), they reported a significant increase and local maximum in skewness, kurtosis, and rogue wave probability from laboratory experiment. Gramstad et al. (2013) use standard boussinesq model with improved dispersion to study the effect of slope length, the shallower water depth and also the effect wave steepness.

Either KdV model or standard boussinesq model is only good for shallow water but not for deep water. On the other hand, the NLS model can handle the wave propagation in deep water but not in shallow water region. In this section, the HOS method is utilized to handle the propagation from deeper water towards shallow water. Third order HOS method with hybrid spatial spectral method is used for all the simulations. In the first subsection, comparison with laboratory experiments are performed to see if HOS method can reproduce the evolution of skewness and kurtosis over a sloping bottom. In the last

subsection, the bottom profile is modified to have different steepness of bottom and also different range of depth ratio between deep and shallow water.

4.5.1 Comparison with laboratory experiments

The experiments were conducted at MARIN in The Netherlands for a benchmark workshop on numerical wave modeling (see Bunnik (2010)). Irregular waves with spectrum of JONSWAP-type and random phases were generated to propagate over a 1:20 slope from water of constant depth 0.6 m to 0.3 m. The distance from the wave generator to the start of the slope was 143.41 m and the slope ended 6 m further. The wave gauges were installed at distances 39.15 m, 78.80 m, 102.12 m, 143.41 m, 146.43 m, 149.41 m, 157.74 m, and 172.89 m from wave maker. In this experiment, three cases of long crested irregular waves were considered as shown in Table 4.6. The statistical properties of this experiment is reported by Trulsen et al. (2012)

Table 4.6: Parameters of the wave-fields in MARIN experiment

Case	**Hs [m]**	**Tp [s]**	$(k_p h)_{deep}$	$(k_p h)_{shallow}$
1	0.06	1.273	1.6	0.99
2	0.06	1.697	1.1	0.70
3	0.06	2.121	0.81	0.54

For each simulation, the statistical properties (kurtosis and skewness) are calculated from time series of length $200T_p$ after all wave components have propagated through the whole domain. The convergence of the statistical quantities with respect to number of runs is investigated and it is observed that using 100 random runs in each case is sufficient to get an accurate result. An example of the convergence of these statistical quantities are shown in Figure 4.16.

Figures 4.17, 4.18, and 4.19 show the comparison of kurtosis and skewness for case 1, 2, and 3 between the numerical simulation and the experiments. The local maxima of kurtosis and skewness close to the end of the slope are reproduced in the numerical simulations. For all three cases, simulation result show a good agreement with the experiments.

4.5.2 Effects of the bottom slope and water depth

In this subsection, only one specific type of irregular wave propagating over a set of different bathymetries is considered. A JONSWAP-type spectrum with significant wave height $H_s = 0.06$ m, peak period $T_p = 1.697$ s is chosen. The bottom slope and different water depth in deeper and shallower water region are varied as shown in Table 4.7. The edge of slope in shallower region is fixed at position $x = 149.41$ m.

For all cases, the numerical simulations are carried out by using HOS method third order with hybrid spatial spectral method in a Monte Carlo approach, where the simulations are performed by different incoming wave field, i.e. it is generated from the same spectrum but with different random phases each time.

The skewness, kurtosis and rogue wave probability are calculated for each case. The rogue wave probability is estimated as the probability that wave height H is larger than

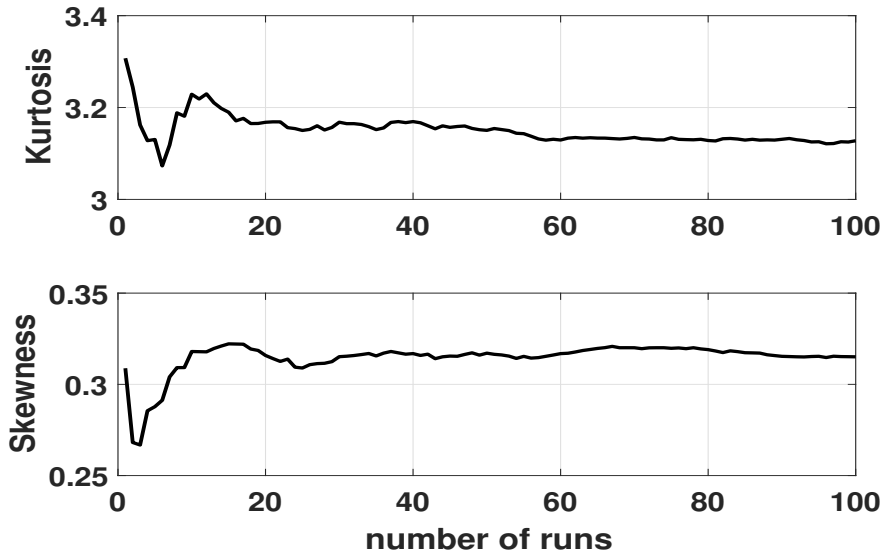

Figure 4.16: Convergence of the ensemble-averaged kurtosis and skewness with respecto to number of runs in the ensemble for case 2.

Table 4.7: Parameters for irregular wave propagation over a sloping bottom simulation. Subscript 1 indicate deeper region, and subscript 2 indicate shallower region.

Case	**Slope length[m]**	h_1**[m]**	h_2**[m]**	$k_p h_1$	$k_p h_2$	**Slope**
I	3	0.6	0.3	1.065	0.696	1/10
II	15	0.6	0.3	1.065	0.696	1/50
III	30	0.6	0.3	1.065	0.696	1/100
IV	45	0.6	0.3	1.065	0.696	1/150
V	45	0.9	0.3	1.415	0.696	1/75
VI	45	1.2	0.3	1.776	0.696	1/50
VII	45	1.8	0.3	2.546	0.696	1/30
VIII	45	2.4	0.3	3.362	0.696	1/21.4

two times significant wave height H_s where $H_s = 4\sigma$ and σ is the standard deviation of the surface elevation. The wave height H is the vertical distance between upper and lower envelopes, and calculated as $H(t) = 2\sqrt{\eta(t)^2 + \tilde{\eta}(t)^2}$, where $\tilde{\eta}(t)$ is the Hilbert transform of $\eta(t)$.

For Case I-IV, the slope length is modified and it is observed in Figure 4.20 and 4.22 that the kurtosis, skewness, and rogue wave probability has local maxima at the end of the slope and it decrease after some distance in shallower region. For large slope length, the local maxima of the statistical quantities disappear as shown in the results of Case IV. For Case V-VIII, it is shown that local maxima of kurtosis and skewness can be observed even with sufficiently large slope length as shown in Figure 4.21. Furthermore, the rogue

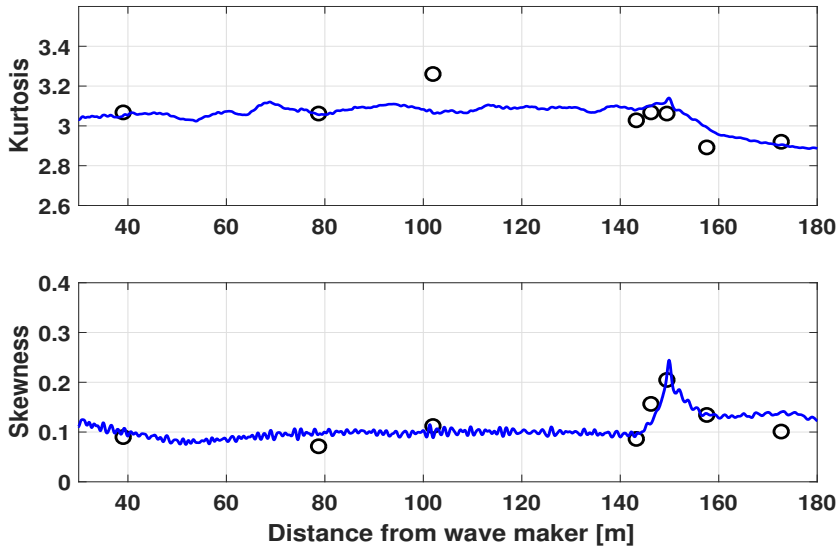

Figure 4.17: Kurtosis and skewness for the experimental case 1. Black circles: experimental results reported by Trulsen et al. (2012), solid line: numerical simulations.

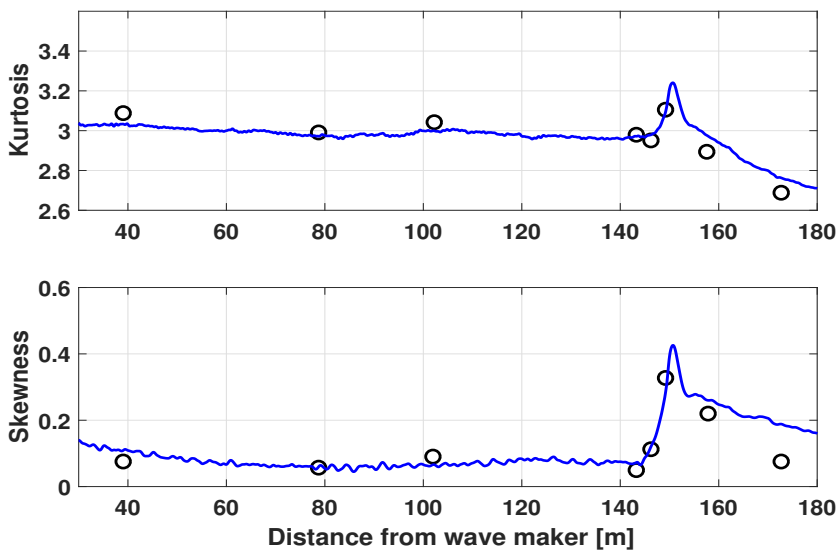

Figure 4.18: Same as Figure 4.17 for experimental case 2.

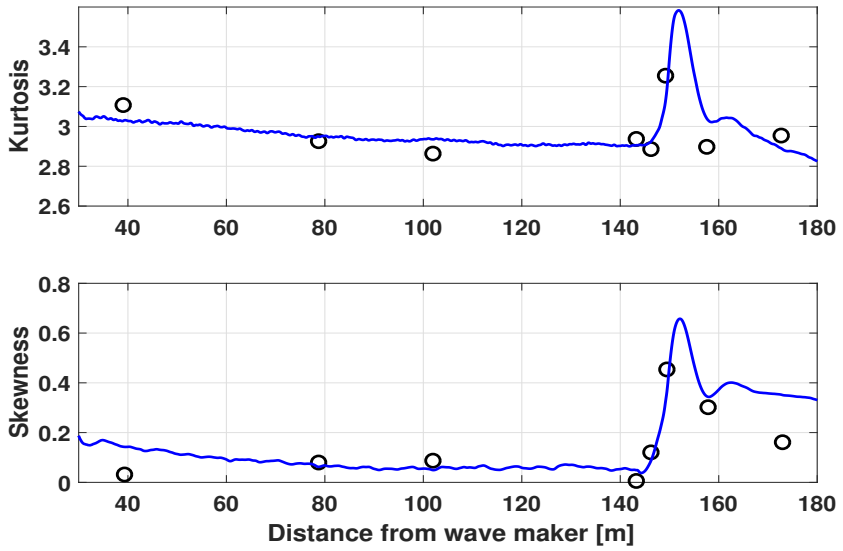

Figure 4.19: Same as Figure 4.17 for experimental case 3.

wave probability of these cases are not that different in terms of magnitude even though the probability is increasing in the slope region (see Figure 4.23).

From these results, it is confirmed that the slope length plays an important role when the water depth is sufficiently small. For propagation from deeper water region towards shallow water, the steepness of the bottom is important for the behaviour of kurtosis and skewness.

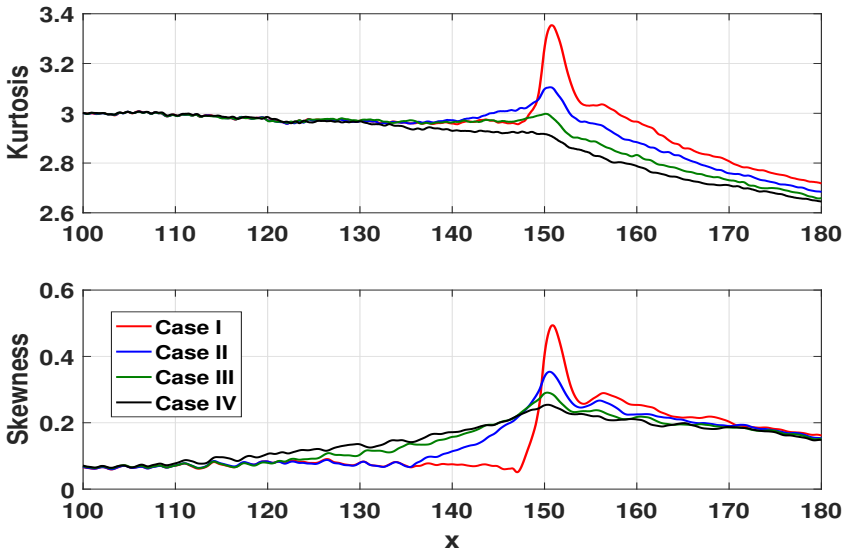

Figure 4.20: Kurtosis and skewness for different slope length cases, i.e. Case I-IV.

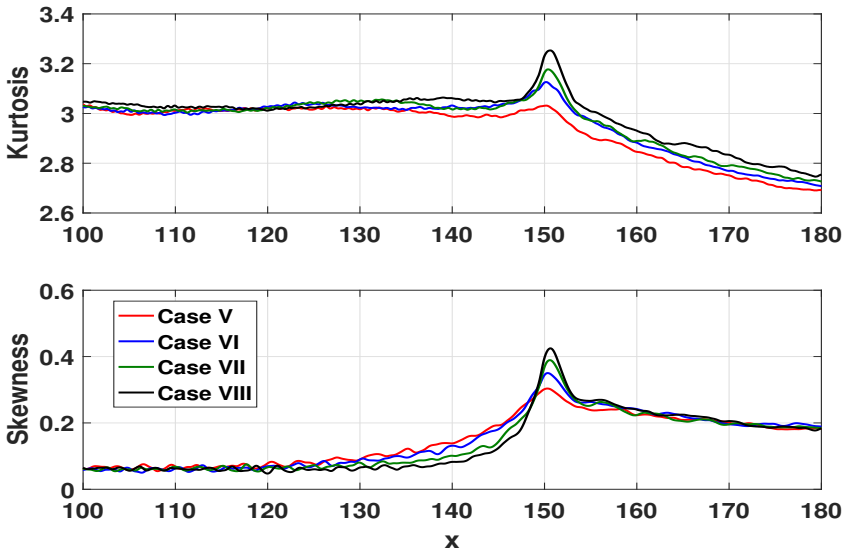

Figure 4.21: Kurtosis and skewness for different water depth cases, i.e. Case V-VIII.

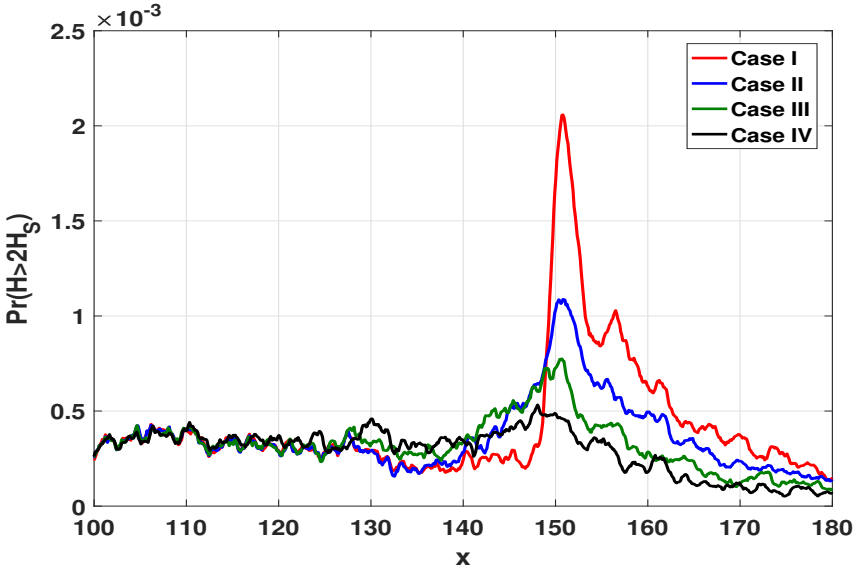

Figure 4.22: Probability of rogue waves for case I-IV.

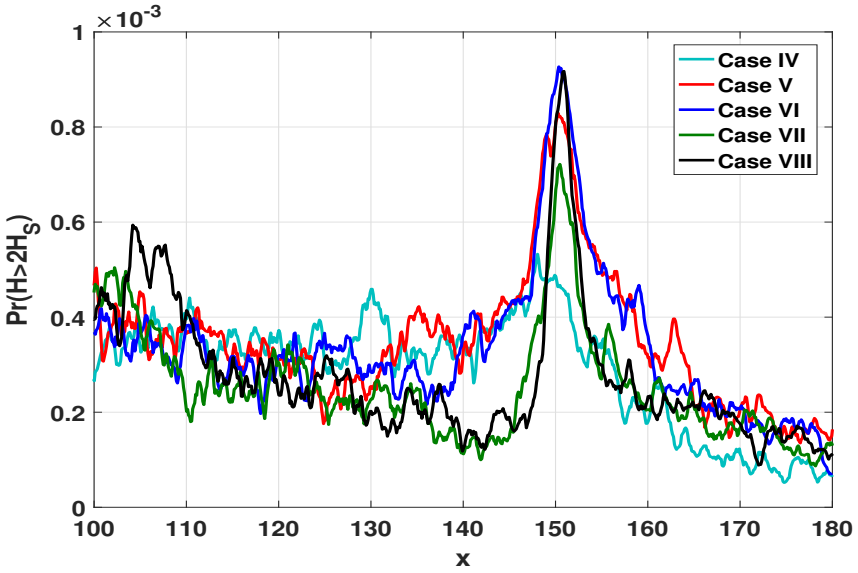

Figure 4.23: Probability of rogue waves for case V-VIII.

Chapter 5

Calculation of Water Particle Kinematics

This chapter describes the calculation of water particle kinematics based on the information at the surface. For Boussinesq-type of equation , the surface elevation η and velocity potential ϕ are calculated at every integration time step. However, the water particle kinematics in the interior domain are needed in many practical applications such as coupling with Computational Fluid Dynamics (CFD) code to deal with breaking waves for instance. The accurate prediction of these kinematics is essential since it is related to force calculation and directly connected with the design of offshore structures. Three different methods will be discussed as follow.

5.1 H and H_2 operator

Two new operators, referred as the H and H_2 operators were introduced in Bateman et al. (2003). The H operator improves the method proposed by Fenton and Rienecker (1982) which transforms any kinematic quantity at the surface to still water level $z = 0$. However the H operator accuracy is related to the convergence of Taylor series therefore the errors arise during the calculation of the kinematics profile beneath the crest of an extreme wave. To remedy this problem, a second operator (H_2 operator) allows the kinematic values on any surface to be transformed onto a second arbitrary surface. It leads the transformation from the surface to $z = 0$ in several small steps. By using sufficiently number of steps, the convergence of the operator is maintained. Brief review of these two operators is given in the following.

Assume an arbitrary kinematic quantity ξ can be represented in Fourier space as follow

$$\xi(\mathbf{x}, z, t) = \int \hat{\xi}(k) \frac{\cosh\,(k(z+h))}{\cosh\,(kh)} e^{i(k\mathbf{x}-\omega t)} dk. \tag{5.1}$$

Equation (5.1) is suitable for kinematic quantity whose profile with depth can be repre-

sented by summation of cosh terms such as velocity potential Φ or horizontal velocity $u = \Phi_{\mathbf{x}}$. For an alternative conjugate variable such as vertical velocity $w = \Phi_z$, the cosh terms in Equation (5.1) should be replaced by sinh.

For H operator, completely analogous with HOS method approach as in Equation (2.12), the kinematic quantity ξ is transformed to $z = 0$ as follow

$$\begin{aligned} \xi^{(1)}(\mathbf{x}, 0, t) &= \xi(\mathbf{x}, \eta, t) \\ \xi^{(m)}(\mathbf{x}, 0, t) &= -\sum_{n=1}^{m-1} \frac{\eta^n}{n!} \frac{\partial^n \xi^{(m-n)}}{\partial z^n}(\mathbf{x}, 0, t), \qquad m \geq 2. \end{aligned} \tag{5.2}$$

For H_2 operator, the kinematic quantity is calculated on a second arbitrary surface $\eta_2 = c\eta$ with c decreasing from 1 to 0. Note that the H_2 operator is equivalent to H operator when $\eta_2 = \eta$. The kinematic quantity at $z = \eta_2$ is expanded by using taylor expansion as

$$\xi^{(m)}(\mathbf{x}, z = \eta_2, t) = \sum_{n=0}^{m-1} \frac{\eta_2^n}{n!} \frac{\partial^n \xi^{(m-n)}}{\partial z^n}(\mathbf{x}, 0, t). \tag{5.3}$$

5.2 Variational Boussinesq Model

As discussed in Chapter 2.1.3, the velocity potential Φ can be expressed explicitly as

$$\Phi(\mathbf{x}, z, t) = \phi(\mathbf{x}, t) + \Sigma_m F_m(z, \eta, h)\, \psi_m(\mathbf{x}, t) = \phi + F \cdot \Psi$$

where F and Ψ are vector functions. The vertical profiles F_m have to be chosen in advance. The normalized hyperbolic-cosine vertical profile in Equation is used in this thesis. The parameters κ_m are optimized based on the given wave spectrum. While the functions ψ_m are determined by minimizing the kinetic energy with respect to ψ_m in order to satisfy the laplace equation.

The horizontal and vertical velocity for VBM are given as follow

$$\begin{aligned} u &= \frac{\partial \Phi}{\partial \mathbf{x}} = \frac{\partial \phi}{\partial \mathbf{x}} + \frac{\partial F}{\partial \mathbf{x}} \cdot \Psi + F \cdot \frac{\partial \Psi}{\partial \mathbf{x}} \\ w &= \frac{\partial \Phi}{\partial z} = \frac{\partial F}{\partial z} \cdot \Psi \end{aligned} \tag{5.4}$$

Other kinematic quantities such as the acceleration or the dynamic pressure can be calculated directly since the velocity potential Φ is expressed explicitly. The calculation of kinematics is relatively easy with this method. However, the function Ψ needs to be calculated every integration time step.

5.3 Nonlinear Extension of Airy Theory

The ansatz of the nonlinear extension of Airy potential to calculate water particle kinematics was introduced in Kurnia and van Groesen (2017). The explicit expression of the

velocity potential is given as

$$\Phi(\mathbf{x}, z, t) = \int \hat{\phi}(k) \frac{\cosh\, k(z+h)}{\cosh\, k(\eta+h)} e^{ik\mathbf{x}} dk. \tag{5.5}$$

The horizontal and vertical velocity are given by the expressions below

$$\begin{aligned} u &= \frac{\partial \Phi}{\partial \mathbf{x}} = \int ik\hat{\phi}(k,t) \frac{\cosh\, k(z+h)}{\cosh\, k(\eta+h)} e^{ik\mathbf{x}} dk + \frac{\partial(\eta+h)}{\partial \mathbf{x}} \cdot \Gamma \\ w &= \frac{\partial \Phi}{\partial z} = \int \hat{\phi}(k,t) \frac{k\, \sinh\, k(z+h)}{\cosh\, k(\eta+h)} e^{ik\mathbf{x}} dk \end{aligned} \tag{5.6}$$

with

$$\Gamma = \int \hat{\phi}(k,t) \frac{\cosh\, k(z+h)}{\cosh\, k(\eta+h)} \left[-k\, \tanh\, k(\eta+h)\right] e^{ik\mathbf{x}} dk.$$

The condition that velocity potential at surface $\Phi(z=\eta)$ is equal to surface potential ϕ is fulfilled in Equation (5.5). Different from VBM, this approach doesn't have any functions that need to be calculated in each time step. Consequently, it is dubious to claim the ansatz fulfill the laplace condition for nonlinear waves. This method only valid for waves with moderate slope and small amplitude since the ansatz use quasi homogeneous way to express the velocity potential Φ explicitly. A counter example for this method to calculate the kinematic on high amplitude wave will be shown in the next section.

5.4 Validation

Kinematic calculation on solitary wave with high amplitude is chosen as a test case in this section. Dutykh and Clamond (2014) give the solitary wave solutions for free surface Euler equations and their solutions will be referred as exact solution in this thesis. The solitary wave has amplitude 0.6 m and water depth 1 m.

The kinematic calculation results at still water level $z = 0$ for the first method which is H and H_2 operator with third order HOS method can be seen in Figure 5.1 and 5.2. Inaccuracy for H operator is expected since the solitary wave has high amplitude. This can be improved by using H_2 operator with increasing number of steps. It is clearly that H_2 operator give a significant improvement from H operator by only using two number of steps. Convergence analysis of horizontal and vertical velocity calculation has been carried out in terms of number of steps and different nonlinearity order, as shown in Figure 5.3 and 5.4. These figures show that the kinematic calculation with H_2 operator converge with approximately less than ten steps and also the error is reduced by increasing nonlinearity order. Velocity profiles for solitary wave by using H_2 operator method are shown in Figure 5.5 and 5.6

For the kinematic calculation with VBM, the horizontal and vertical velocity at $z = 0$ are in a good agreement with the exact solution as shown in Figure 5.7. The root mean square errors of horizontal and vertical velocity are 1.3×10^{-4} and 5.2×10^{-4} respectively.

For nonlinear extension of airy theory, comparison of vertical velocity at surface with exact solution is given in Figure 5.8. From this figure, it is enough to observe that this method is inaccurate for high amplitude waves. The vertical velocity at the surface can be obtained directly from HOS method which means this is the easiest case.

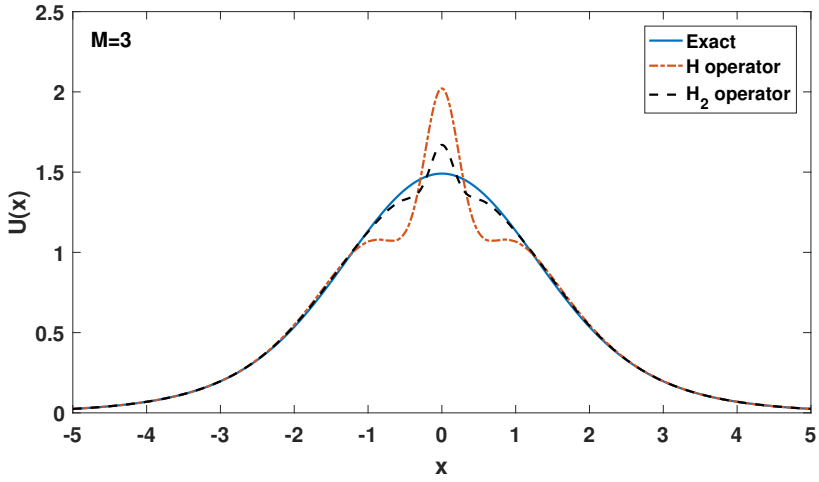

Figure 5.1: Comparison of horizontal velocity at $z = 0$ betwen H and H_2 operator with exact solution. The H_2 operator is performed by two steps.

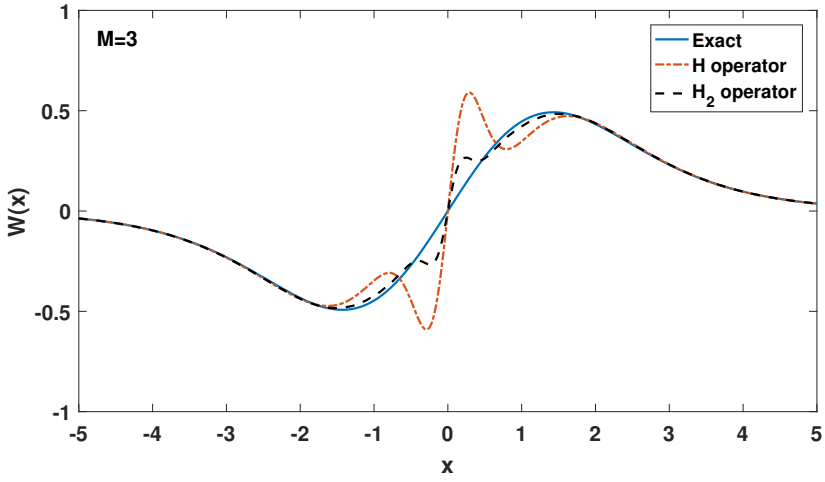

Figure 5.2: Same as Figure 5.1, now for vertical velocity

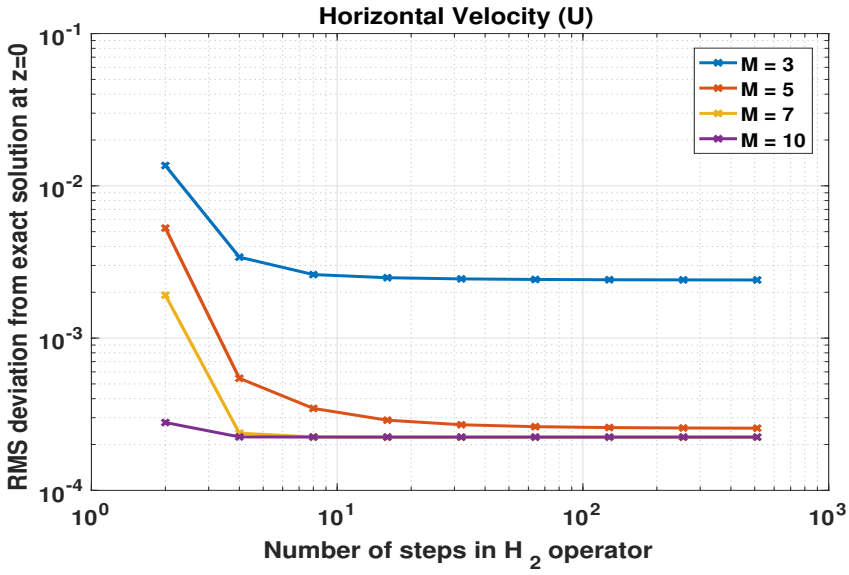

Figure 5.3: Convergence of horizontal velocity with respect to number of steps in H_2 operator for different degrees of nonlinearity.

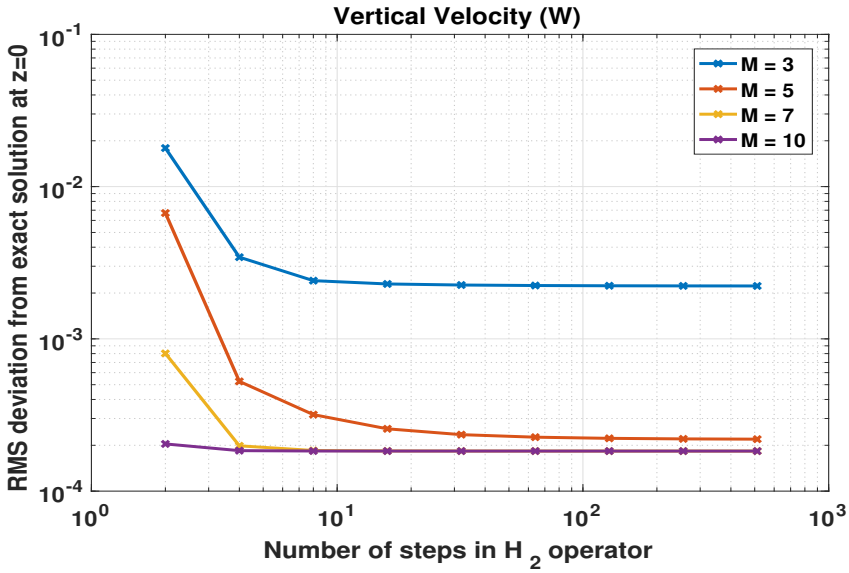

Figure 5.4: Same as Figure 5.3, now for vertical velocity.

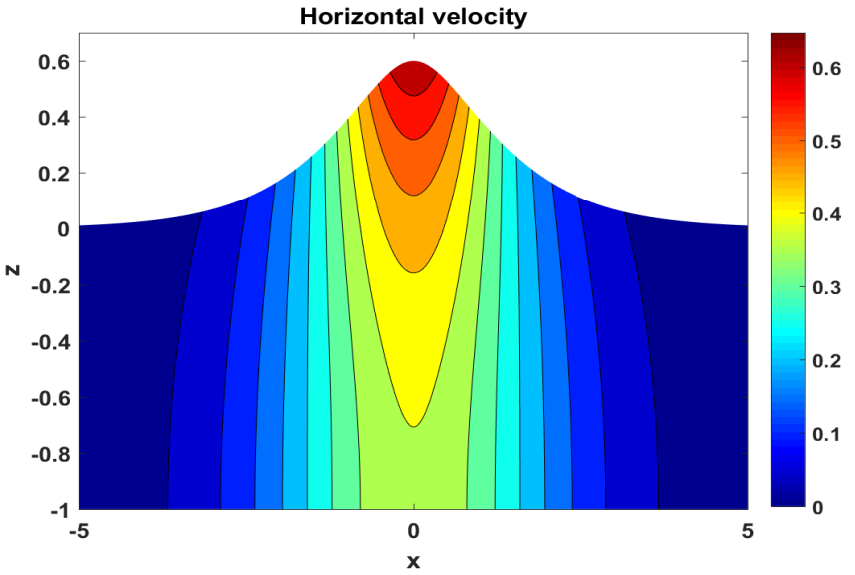

Figure 5.5: Horizontal velocity profile of a solitary wave by using H_2 operator.

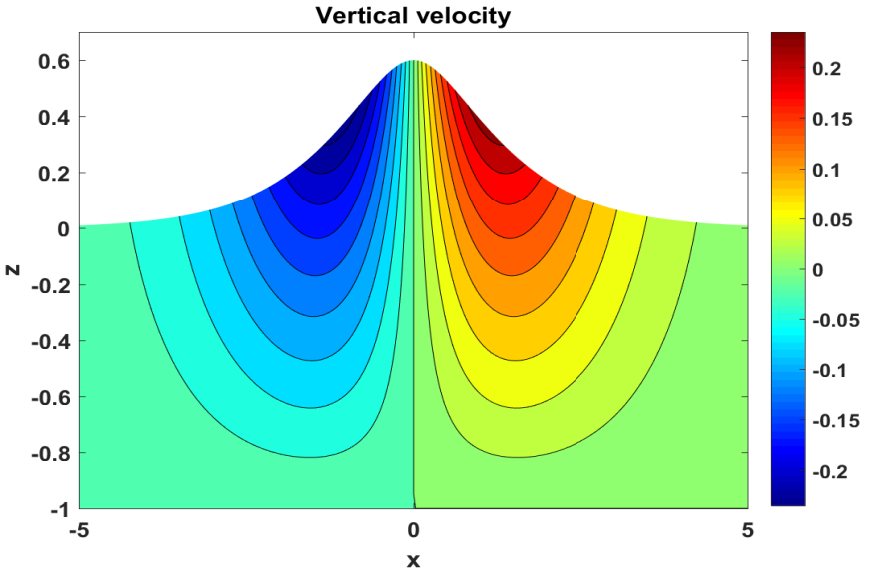

Figure 5.6: Vertical velocity profile of a solitary wave by using H_2 operator.

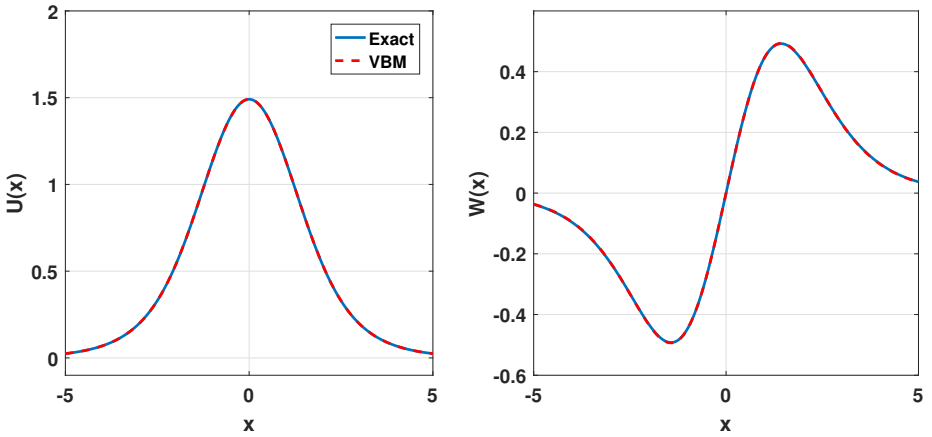

Figure 5.7: Comparison of horizontal and velocity at $z = 0$ between VBM method and exact solution.

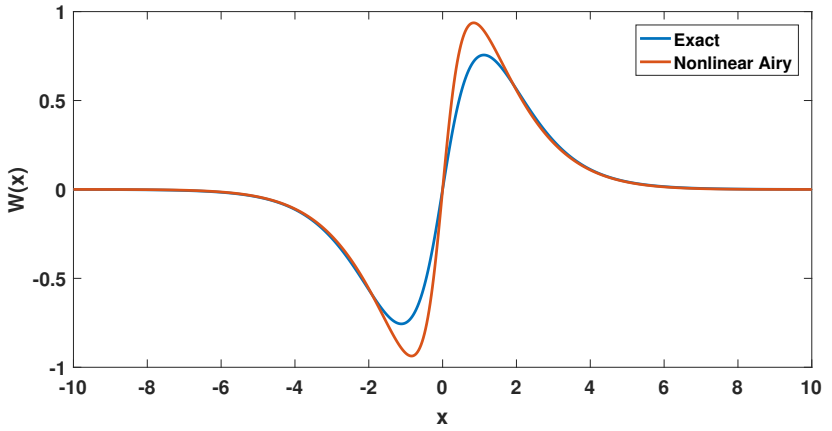

Figure 5.8: Comparison of vertical velocity at surface between nonlinear extension of airy theory and exact solution.

Chapter 6

Conclusion and recommendations

6.1 Conclusion

The important aspects in wave modeling are the frequency dispersion and the nonlinearity. The frequency dispersion is the relation that describe the speed of the wave propagation at different wave length. In this aspect, the nonlinearity describe the phenomenon that there is energy exchange between different wave modes that can lead to steeper waves.

Two wave models based on Hamiltonian formulation are considered and implemented in different numerical methods. The High Order Spectral (HOS) method is valid for any uniform depth, and the order of nonlinearity can be increased to deal with high steep waves. The pseudo spectral implementation on HOS method give an efficient computational time and accurate dispersion which is essential in predict the wave propagation at sea. For comparison, the Variational Boussinesq Model (VBM) which is included in software package HAWASSI is utilized to study the performance of HOS method. The VBM has parameters that can be tuned to approximate the dispersion based on kinetic energy minimization. Furthermore, the VBM has a fully nonlinear model and it is implemented in finite element method for both 1D and 2D in the software HAWASSI-VBM.

In order to be able to study the wave model from wave tank experiment, wave generation in wave model is needed to see the evolution of the waves. As in HAWASSI software, embedded wave generation is adapted and implemented in HOS method. Furthermore, the HOS method is extended to handle varying bottom successfully with two different methods.

A solitary wave with high nonlinearity ($a/h_0 = 0.7$) is simulated with different order nonlinearity in HOS method. The HOS method simulation results converge to fully nonlinear VBM which show the importance of dispersion and nonlinearity to maintain the shape of the solitary wave. Subsequently, this case also proof that the Hamiltonian wave model possess the property of energy conservation.

The bichromatic wave train experiment is chosen to study the nonlinear interaction between modes. In the propagation of bichromatic waves, the side frequency modes are generated due to third order effect. As expected, the HOS method first and second order

are fail to predict the generation of side frequency modes. In this case, HOS third order give a satisfactory results compared to the experiment data.

A focusing wave group experiment is chosen to study the nonlinear interaction in broad band spectrum. This experiment was designed to be focused at a certain position based on linear theory. However, in reality the nonlinearity plays an important role when dealing with the high amplitude waves. In this experiment, some white capping was observed about the focusing point which means this focusing wave experiment has strong nonlinearity. The HOS first order simulation predicts the focused point exactly the same with the initial design but the spectrum from the measurement data show that the initial spectrum is deformed in tail part and the linear simulation fail to predict the energy transfer to the spectrum tail. Subsequently, the HOS third order give a better results and produce higher and steeper focused wave compared to the linear simulation.

For non-uniform bathymetry, HOS method is tested against wave propagation over a submerged bar. Both original and hybrid spatial spectral method work very well. Apparently, the hybrid spatial spectral method has a huge advantage in terms of computational time. However, the FIO interpolation should be done carefully to get accurate result.

The study in irregular waves propagation from deep to shallow water over a sloping bottom has been done with comparison against laboratory experiment and several numerical cases. In this case, the validation with experimental data show a good agreement in terms of statistical quantities (kurtosis and skewness). Furthermore, it is found that the bottom slope is an important parameter for the statistical quantities including the probability of rogue waves.

Finally, the calculation of water particle kinematics are described and validated against exact solution. This calculation allows the HOS method to be coupled with other CFD codes to handle wave-body interaction or other difficult cases such as breaking waves.

6.2 Recommendations

The following problems are recommended for future research related to the work of this thesis.

- It is useful to study further the interpolation technique to calculate the Fourier integral operator (FIO) in hybrid spatial spectral method.
- The present HOS method is implemented for long crested waves only. It is interesting to extend the HOS method into 3D framework to study the occurence of rogue waves over bathymetry with short-crest waves.

Bibliography

Adytia, D., 2012. Coastal zone simulations with variations Boussinesq modelling (Ph.D. thesis). University of Twente, Enschede, The Netherlands.

Adytia, D., van Groesen, E., 2012. Optimized variational 1d boussinesq modelling of coastal waves propagating over a slope. Coastal Engineering 64, 139 – 150.

Alber, I., 1978. The effects of randomness on the stability of two-dimensional surface wavetrains. Proceedings of the Royal Society of London A: Mathematical, Physical and Engineering Sciences 363 (1715), 525–546.

Bateman, W., Swan, C., Taylor, P., 2003. On the calculation of the water particle kinematics arising in a directionally spread wavefield. Journal of Computational Physics 186, 70–92.

Beji, S., Battjes, J., 1993. Experimental investigation of wave propagation over a bar. Coast. Eng. 19, 151–162.

Benjamin, T. B., Feir, J. E., 1967. The disintegration of wave trains on deep water. Part 1. Theory. Journal of Fluid Mechanics 27, 417–430.

Berkhoff, J., Booy, N., Radder, A., 1982. Verification of numerical wave propagation models for simple harmonic linear water waves. Coastal Engineering 6 (3), 255 – 279.

Bogacki, P., Shampine, L. F., 1989. A 3(2) pair of runge-kutta formulas. Appl. Math. Letters 2, 321–325.

Broer, L. J. F., Jan 1974. On the hamiltonian theory of surface waves. Applied Scientific Research 29 (1), 430–446.

Bunnik, T., 2010. Benchmark workshop on numerical wave modelingdescription of test cases. MARIN Technical Report 700221 RD.

Craig, W., Guyenne, P., Nicholls, D., Sulem, C., 2005. Hamiltonian long-wave expansions for water waves over a rough bottom. Roy. Soc., 839–873.

Dommermuth, D., 2000. The initialization of nonlinear waves using an adjustment scheme. Wave Motion 32 (4), 307 – 317.

Dommermuth, D. G., Yue, D. K. P., 1987. A high-order spectral method for the study of nonlinear gravity waves. Journal of Fluid Mechanics 184, 267–288.

Dutykh, D., Clamond, D., 2014. Efficient computation of steady solitary gravity waves. Wave Motion 51 (1), 86 – 99.

Dysthe, K., Krogstad, H. E., Mller, P., 2008. Oceanic rogue waves. Annual Review of Fluid Mechanics 40 (1), 287–310.

Engquist, B., Majda, A., 1977. Absorbing boundary conditions for numerical simulation of waves. Proceedings of the National Academy of Sciences 74 (5), 1765–1766.

Fenton, J., Rienecker, M., 1982. A fourier method for solving nonlinear water-wave problems: application to solitary-wave interactions. J. Fluid Mech. 118, 411–443.

Gouin, M., Ducrozet, G., Ferrant, P., 2016. Development and validation of a non-linear spectral model for water waves over variable depth. European Journal of Mechanics B/Fluids 57, 115–128.

Gramstad, O., 2017. Modulational instability in jonswap sea states using the alber equation. International Conference on Offshore Mechanics and Arctic Engineering 7B.

Gramstad, O., Trulsen, K., 2007. Influence of crest and group length on the occurrence of freak waves. Journal of Fluid Mechanics 582, 463472.

Gramstad, O., Zeng, H., Trulsen, K., Pedersen, G., 2013. Evolution of skewness and kurtosis of weakly nonlinear unidirectional waves over a sloping bottom. Physics of Fluid 25, 122103.

Guyenne, P., Nicholls, D., 2007. A high-order spectral method for nonlinear water waves over moving bottom topography. J. Sci. Comput 30, 81–101.

Haver, S., 2000. Evidences of the existence of freak waves. Proc. Rogue Waves, 129–140.

Kharif, C., Pelinovsky, E., 2003. Physical mechanisms of the rogue wave phenomenon. European Journal of Mechanics - B/Fluids 22 (6), 603 – 634.

Kim, G., Lee, C., Suh, K.-D., 2007. Internal generation of waves: Delta source function method and source term addition method. Ocean Engineering 34 (17), 2251 – 2264.

Klopman, G., 2010. Variational Boussinesq modelling of surface gravity waves over bathymetry (Ph.D. thesis). University of Twente, Enschede, The Netherlands.

Klopman, G., Van Groesen, E., Dingemans, M. W., 2010. A variational approach to boussinesq modelling of fully nonlinear water waves. Journal of Fluid Mechanics 657, 36–63.

Kurnia, R., van Groesen, E., 2014. High order hamiltonian water wave models with wave-breaking mechanism. Coastal Engineering 93, 55–70.

Kurnia, R., van Groesen, E., 2017. Localization for spatialspectral implementations of 1d analytic boussinesq equations. Wave Motion 72, 113–132.

Lakhturov, I., Adytia, D., van Groesen, E., 2012. Optimized variational 1d boussinesq modelling for broad-band waves over flat bottom. Wave Motion 49, 309 – 322.

Lawrence, C., Adytia, D., van Groesen, E., 2018. Variational boussinesq model for strongly nonlinear dispersive waves. Wave Motion 76, 78 – 102.

Liam, L. S., Adytia, D., van Groesen, E., 2014. Embedded wave generation for dispersive surface wave models. Ocean Engineering 80, 73 – 83.

Liam, S. L., 2013. Mathematical modelling of generation and forward propagation of dispersive waves (Ph.D. thesis). University of Twente, Enschede, The Netherlands.

Liu, Y., Yue, D., 1998. On generalized bragg scattering of surface waves by bottom ripples. J. Fluid Mech. 356, 297–326.

Luke, J. C., 1967. A variational principle for a fluid with a free surface. Journal of Fluid Mechanics 27 (2), 395–397.

Madsen, P. A., Murray, R., Srensen, O. R., 1991. A new form of the boussinesq equations with improved linear dispersion characteristics. Coastal Engineering 15 (4), 371 – 388.

Miles, J. W., 1977. On hamilton's principle for surface waves. Journal of Fluid Mechanics 83 (1), 153–158.

Nwogu, O., 1993. Alternative form of boussinesq equations for nearshore wave propagation. Journal of Waterway, Port, Coastal, and Ocean Engineering 119 (6), 618–638.

Peregrine, D. H., 1967. Long waves on a beach. Journal of Fluid Mechanics 27 (4), 815–827.

Sergeeva, A., Pelinovsky, E., Talipova, T., 2011. Nonlinear random wave field in shallow water: Variable korteweg-de vries framework. Nat. Hazards Earth Syst. Sci. 11, 323–330.

Stansberg, C. T., 1998. On the nonlinear behaviour of ocean wave groups. In: Proc. Third International Symposium on Ocean Wave Measurement and Analysis. Vol. 2. pp. 1227–1241.

Trulsen, K., Stansberg, C. T., 2001. Spatial evolution of water surface waves: Numerical simulation and experiment of bichromatic waves. In: International Offshore and Polar Engineering Conference.

Trulsen, K., Zeng, H., Gramstad, O., 2012. Laboratory evidence of freak waves provoked by non-uniform bathymetry. Physics of Fluid 24, 097101.

van Groesen, E., Andonowati, 2011. Fully dispersive dynamic models for surface water waves above varying bottom, part 1: Model equations. Wave Motion 48, 658–667.

van Groesen, E., Turnip, P., Kurnia, R., 2017. High waves in draupner seaspart 1: numerical simulations and characterization of the seas. Journal of Ocean Engineering and Marine Energy 3, 233245.

van Groesen, E., van der Kroon, I., 2012. Fully dispersive dynamic models for surface water waves above varying bottom, part 2: Hybrid spatial-spectral implementations. Wave Motion 49, 198–211.

van Groesen, E., Wijaya, A. P., 2017. High waves in draupner seaspart 2: Observation and prediction from synthetic radar images. Journal of Ocean Engineering and Marine Energy 3, 325332.

Wei, G., Kirby, J. T., 1995. Time-dependent numerical code for extended boussinesq equations. Journal of Waterway, Port, Coastal, and Ocean Engineering 121 (5), 251–261.

Wei, G., Kirby, J. T., Sinha, A., 1999. Generation of waves in boussinesq models using a source function method. Coastal Engineering 36 (4), 271 – 299.

West, B. J., Brueckner, K. A., Janda, R. S., Milder, D. M., Milton, R. L., 1987. A new numerical method for surface hydrodynamics. Journal of Geophysical Research: Oceans 92 (C11), 11803–11824.

Zakharov, V. E., 1968. Stability of periodic waves of finite amplitude on the surface of a deep fluid. Journal of Applied Mechanics and Technical Physics 9 (2), 190–194.

Zeng, H., Trulsen, K., 2012. Evolution of skewness and kurtosis of weakly nonlinear unidirectional waves over a sloping bottom. Nat. Hazards Earth Syst. Sci. 12, 631–638.

Appendix

A Supplementary of simulation results

HOS first order simulation on bichromatic wave group experiment

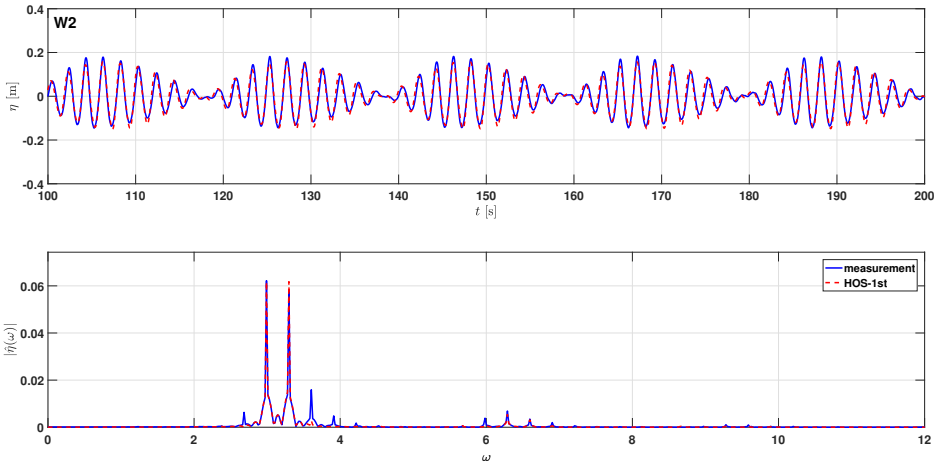

Figure A.1: Comparison of wave elevation (upper plot) and amplitude spectrum (lower plot) for bichromatic wave train experiment between HOS first order (red, dash) and measurement (blue,solid) at position W2 ($x = 40$ m).

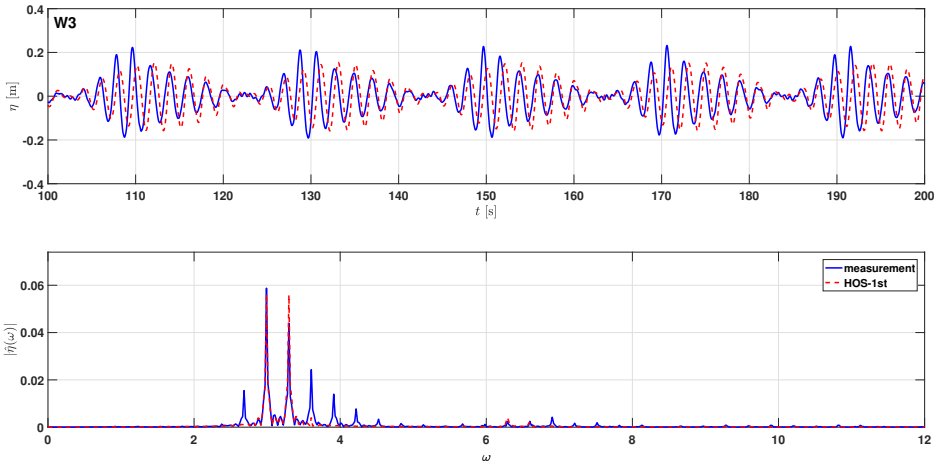

Figure A.2: Same as Figure A.1. Now at position W3 ($x = 80$ m).

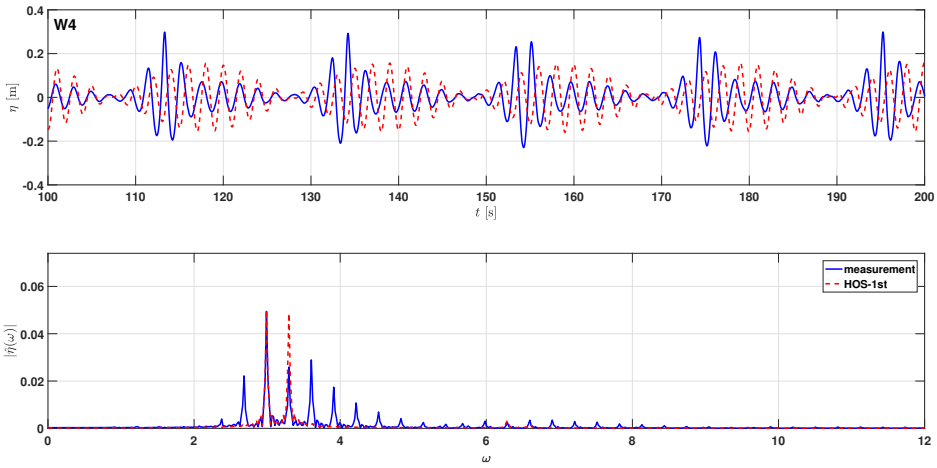

Figure A.3: Same as Figure A.1. Now at position W4 ($x = 120$ m).

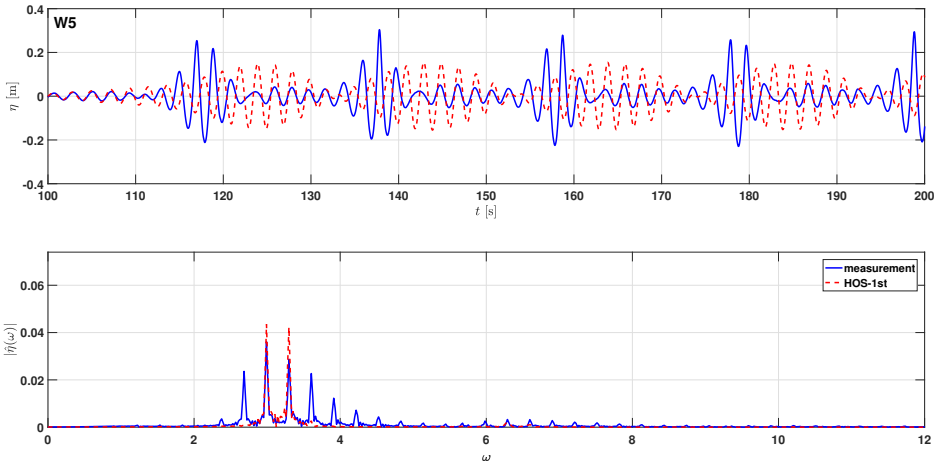

Figure A.4: Same as Figure A.1. Now at position W5 ($x = 160$ m).

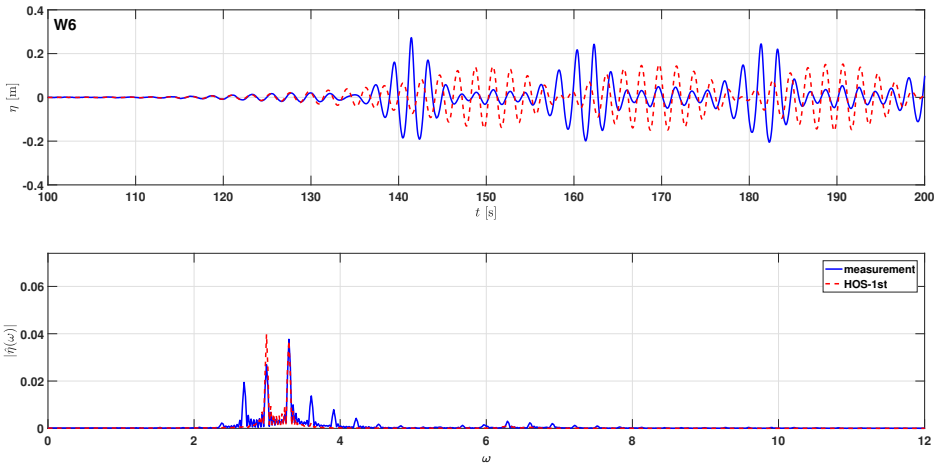

Figure A.5: Same as Figure A.1. Now at position W6 ($x = 200$ m).

HOS second order simulation on bichromatic wave group experiment

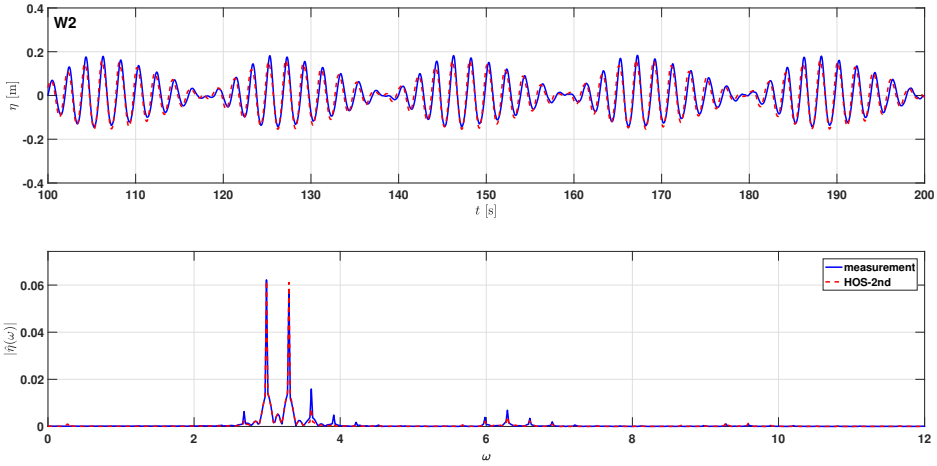

Figure A.6: Comparison of wave elevation (upper plot) and amplitude spectrum (lower plot) for bichromatic wave train experiment between HOS second order (red, dash) and measurement (blue,solid) at position W2 ($x = 40$ m).

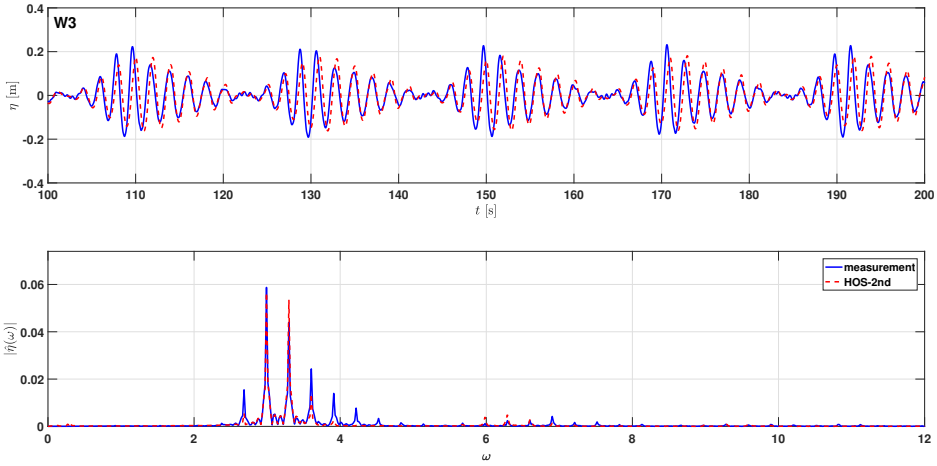

Figure A.7: Same as Figure A.6. Now at position W3 ($x = 80$ m).

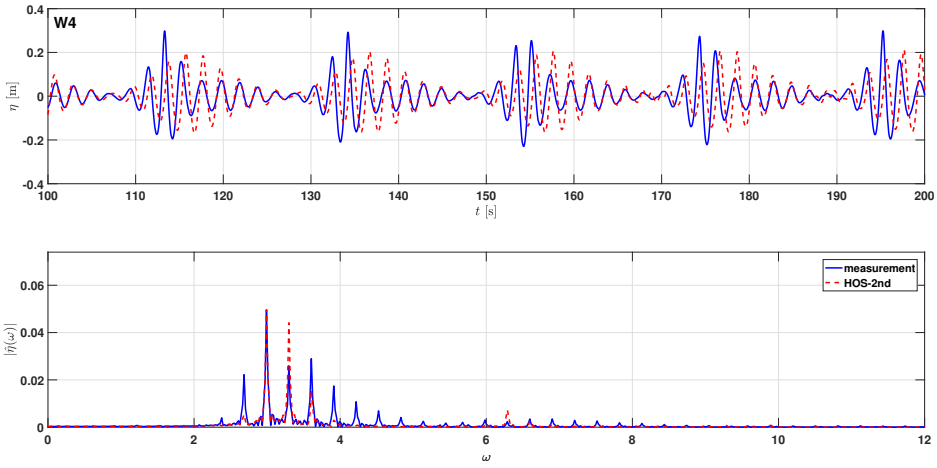

Figure A.8: Same as Figure A.6. Now at position W4 ($x = 120$ m).

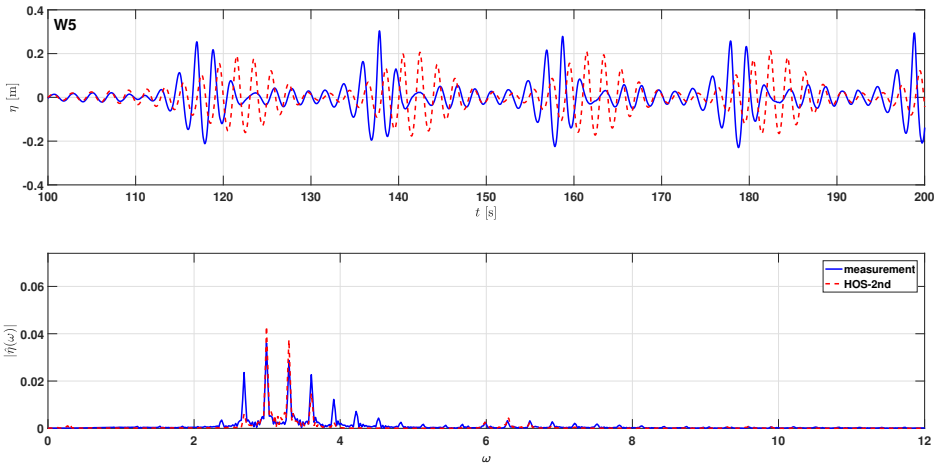

Figure A.9: Same as Figure A.6. Now at position W5 ($x = 160$ m).

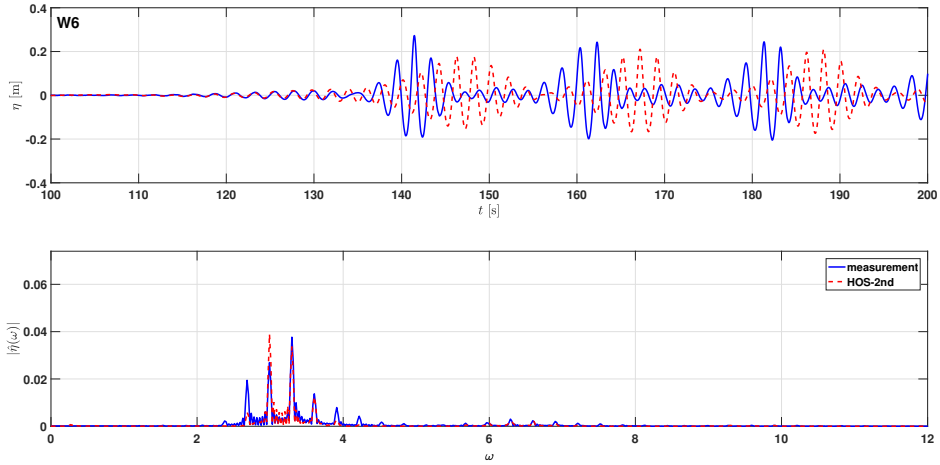

Figure A.10: Same as Figure A.6. Now at position W6 ($x = 200$ m).

Focusing wave group experiment

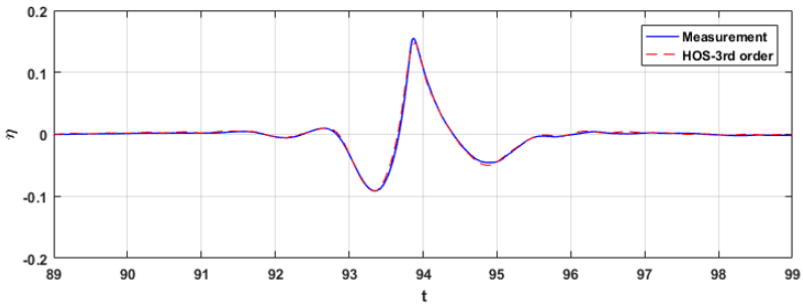

Figure A.11: Comparison of wave elevation for focusing wave group experiment between HOS 3rd order (red, dash) at $x = 50.2$ m and measurement (blue, solid) at $x = 50$ m.

HOS second order simulation on irregular waves over a submerged bar experiment

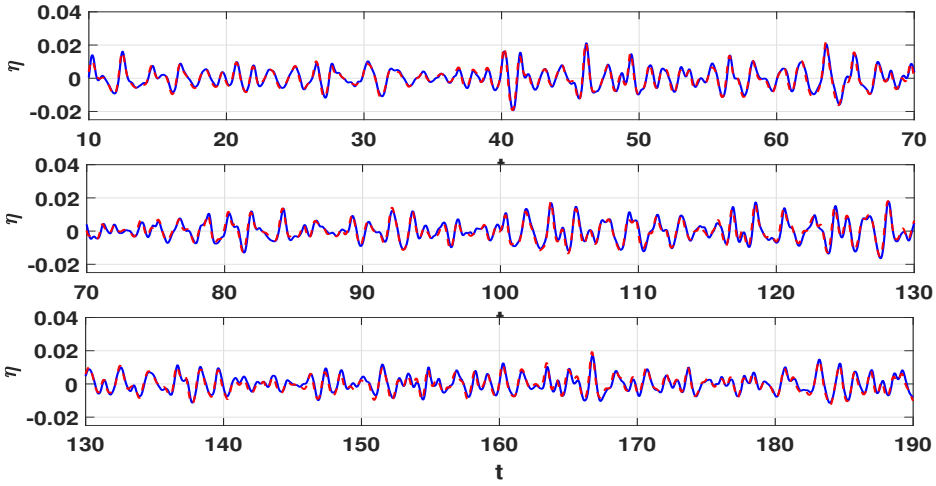

Figure A.12: Comparison of wave elevation for irregular waves over a submerged bar experiment between HOS second order (red, dash) and measurement (blue, solid) at position W2.

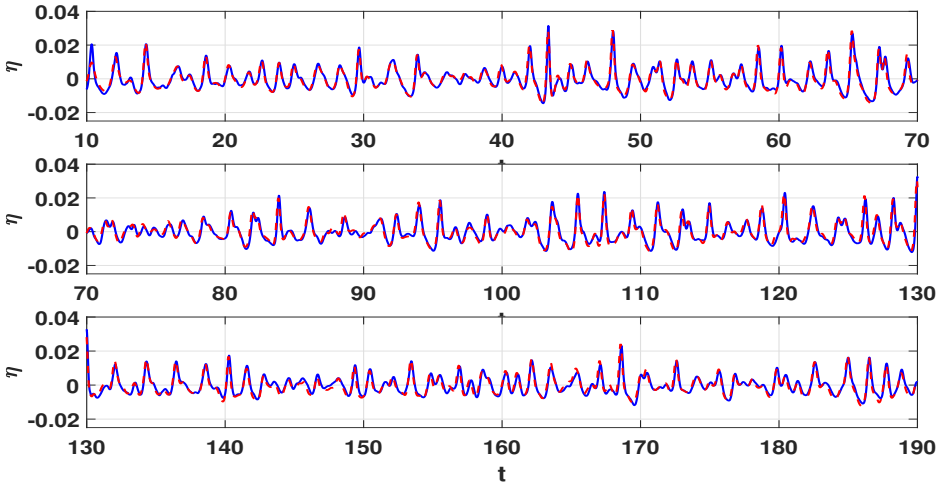

Figure A.13: Same as Figure A.12, now at position W3.

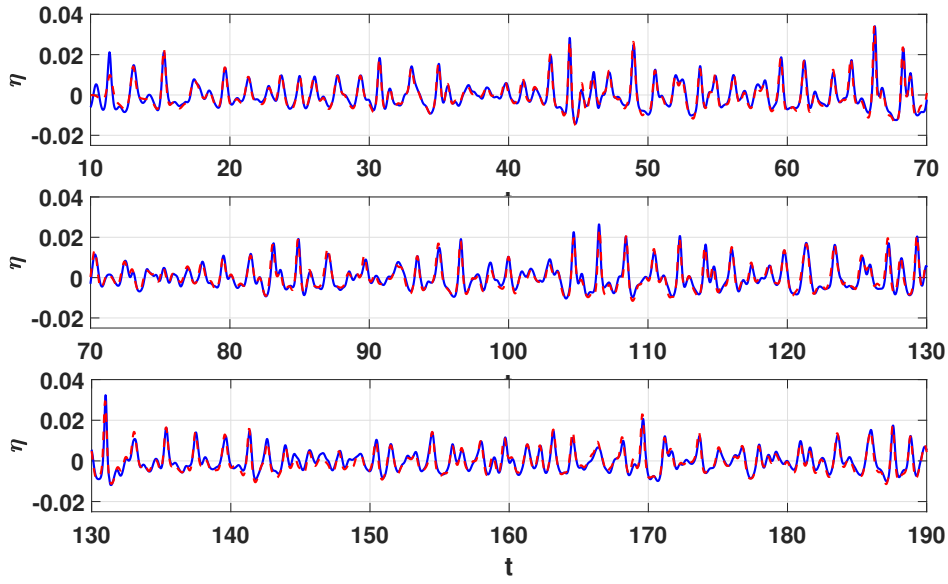

Figure A.14: Same as Figure A.12, now at position W4.

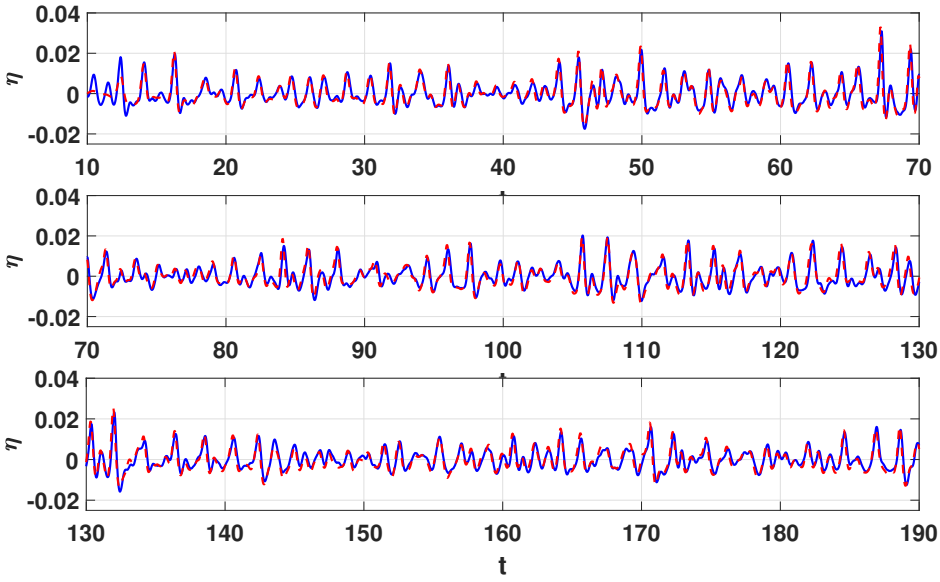

Figure A.15: Same as Figure A.12, now at position W5.

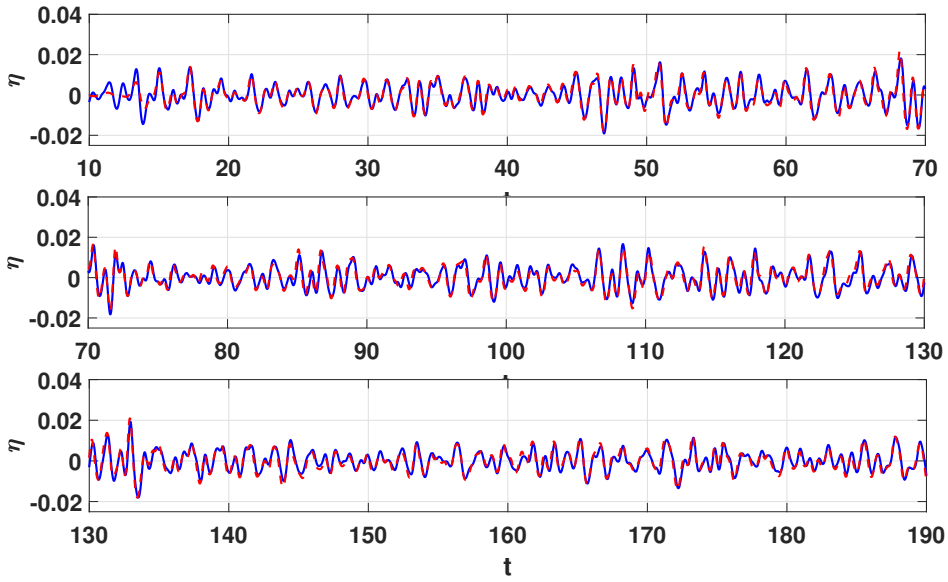

Figure A.16: Same as Figure A.12, now at position W6.

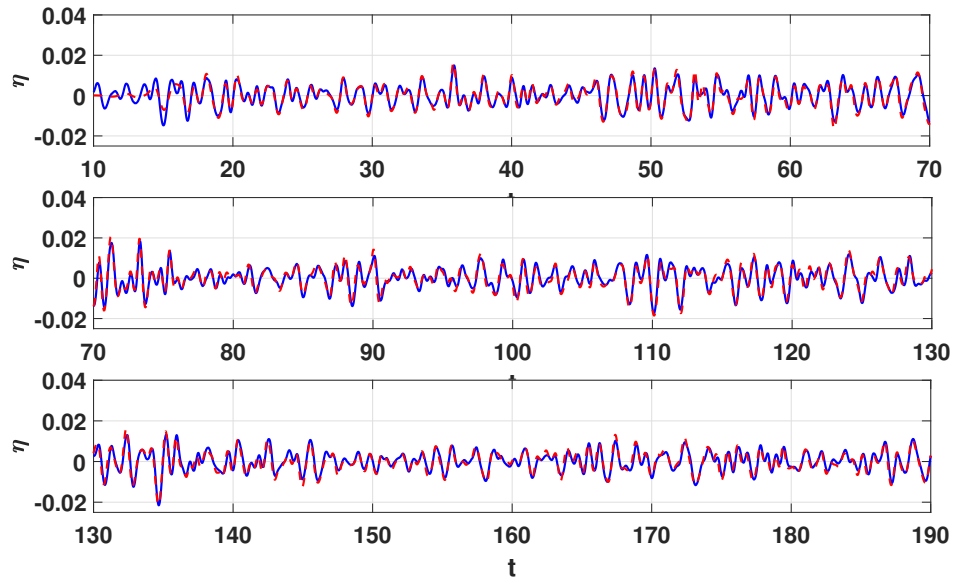

Figure A.17: Same as Figure A.12, now at position W7.